Atomic force microscopy[*]

Jason P. Killgore and Teresa L. Kirschling

Applied Chemicals and Materials Division, National Institute of Standards and Technology,

Boulder, CO 80305

I. What does the technique do?

The atomic force microscope (AFM)[1] has become a universal tool for performing nanoscale

characterization of surfaces. It has the resolution to image features as small as individual atoms

[2], while still providing the range to investigate samples as large as several millimeters [3]. The

AFM is part of a class of instruments known as scanning probe microscopes that also includes

techniques such as scanning tunneling microscopy [4] and scanning near field optical

microscopy [5] in addition to the more widely used atomic force microscopy. The AFM consists

of a cantilever based sensor that is capable of detecting and responding to various forces that

may arise between the sample and a sharpened tip located near the apex of the cantilever. The

instrument has proven capable of measuring a broad range (in both magnitude and origin) of

forces for a wide variety of applications. The earliest uses of the AFM were for topographic

imaging of a sample surface. An image is created by scanning the cantilever tip back and forth

across the sample (in a raster pattern), while recording the height of the surface. Compared to

other techniques such as electron microscopies and tunneling microscopy with comparable

spatial resolution, the AFM excels in its ability to image both conducting and insulating

materials. The instrument is also capable of performing localized spectroscopy measurements

and capturing spatially resolved maps of functional properties such as conductivity [6], elasticity [7] and adhesion [7].

II. Why is getting this information useful?

The nanoscale structures and properties of membranes play an integral role in determining membrane performance. Whether the interest is in determining pore size [8] for molecular weight cut-off studies, or measuring colloidal interactions for fouling prediction [9], the AFM currently plays a critical role in membrane characterization. The AFM has become a standard tool for measuring surface roughness [10-20] and pore size distributions [21-28] of membranes. Extensions of the technique have been used to measure ion and proton flow [29-34], thermal properties [35-37], adhesive properties [9, 11, 38-42], and mechanical heterogeneity [43-47]. The tool also has extensive environmental capabilities that make it particularly useful to membrane studies. This chapter will describe the basics of AFM operation and examine a number of membrane specific applications. It will primarily focus on applications to nanofiltration and reverse osmosis membranes, but will also give examples in gas separation and fuel cells.

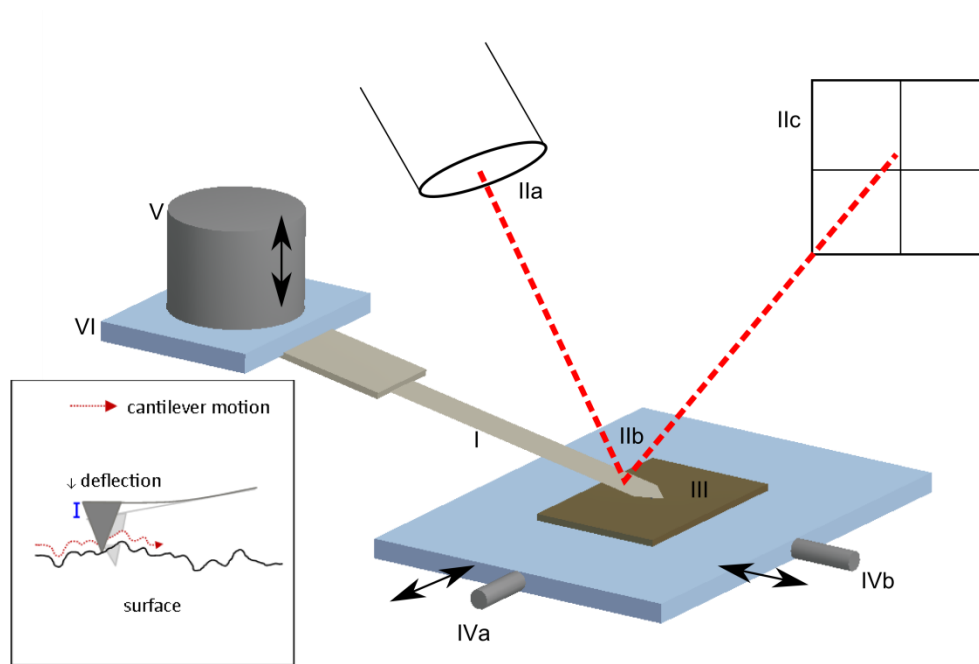## III. Description of the instrument

Figure #.1 Simplified schematic of the AFM. The labels denote different components of the AFM: I – the cantilever, IIa – the laser, IIc – the photodetector, III – the sample, IVa and IVb – the x and y direction positioning piezos, respectively, V – the z actuator and VI – The high frequency dithering piezo. Inset shows a graphic of a tip scanning a rough surface. The inset shows an example of a cantilever scanning a sample surface. The lighter silhouetted cantilever in the background shows the cantilever's undeflected shape if it were in free space. When engaged with the surface, the cantilever deflects upwards.

IIIa. Key parts of the instrument

The AFM instrument is a relatively simple tool given its resolution and versatility. A simplified schematic of a typical instrument (not to scale) is shown in figure #.1 and the key functions of each element are discussed below.
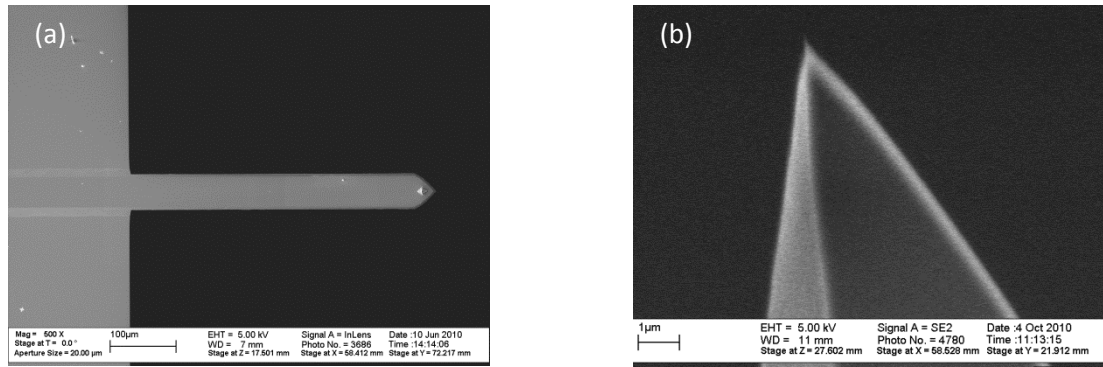
Figure #.2 Scanning electron microscopy image of (a) an AFM cantilever and (b) a higher magnification image of the AFM tip.

At the heart of the AFM is a cantilever sensor for detecting force. The cantilever (I) can deflect under load, and that deflection is approximately proportional to the force between the cantilever and the sample. Early cantilevers were custom made from a metallic foil with a diamond shard glued to the end to serve as the tip. Advances in silicon microfabrication technology [48-50] have resulted in today's low cost, commercial probes and played a large part in the successful adoption of the instrument. The modern cantilevers have a sharpened tip (figure #.2) located near the cantilever apex. The cantilevers and tips are typically made of silicon or silicon nitride, but more exotic materials such as ultrananocrystalline diamond have also been employed [51]. It is also possible for the tip to be coated for wear resistance, chemical compatibility, or electrical conductivity.   Typical tips are 5 μm to 10 μm tall, roughly pyramidal in shape, and terminate with radii from 5 nm to 20 nm. Specialty tip shapes are also available including high aspect ratio tips for imaging of deep pores and trenches, and flared-side tip for sidewall imaging. The cantilevers are typically defined by their stiffness or spring constant (in N/m). This value refers to the force required to deflect a cantilever a certain

4

distance. The spring constant can be tailored to match specific samples and imaging methods, with typical cantilever spring constants ranging from 0.001 N/m for soft biological materials imaged in liquid to 50 N/m for operation in air on rigid inorganic materials.

Once a suitable cantilever has been chosen, it is necessary to sensitively detect the deflection and vibration of the cantilever. Most commercial AFMs use an optical detection system whereby a laser (IIa) is reflected from the back of the cantilever (IIb) and the displacement of the reflected beam is measured by a four-quadrant photodetector (IIc). The photodetector can detect both flexural and torsional deflection of the cantilever. In addition to optical detection, custom systems have been developed to use interferometric detection [52] and self-sensing cantilevers [53].

To trace the topography of the surface and produce an image requires a means of rastering the tip across the sample (III) in x and y (IVa and IVb) directions, while also controlling z-displacement (V) of the cantilever base. This motion is achieved with precise nanopositioners that can be housed in the head or base of the AFM instrument. Most commonly, piezoelectric actuators are used to provide independent or software decoupled x, y and z motion. The AFM has two scan axes, one in the fast out and back direction, and one in a slow scan direction as the scan line traverses down the image area. The direction of these two axes relative to the orientation of the cantilever is typically user selectable. It is common to have a z-range from 5 μm to 15 μm and an x-y range of 10 μm to 100 μm. Larger x-y range can be accommodated with coarse-positioning motors. Often, compromises are made between range and sensitivity, with the highest-resolution tools giving up x, y and z range to ensure optimal performance.

Finally, most AFMs will also provide a means of vibrating the cantilever at high frequencies (tens of kilohertz to few megahertz). This vibration is typically achieved with a high-frequency piezo actuator located above the cantilever mounting point (VI). The actuator is used in a wide number of dynamic AFM methods that are described in more detail below.

All of these AFM components are managed with a sophisticated controller that is capable of monitoring the photodetector, powering the actuators, and providing a feedback loop for imaging. Users are provided the option to tune the individual gains of the proportional-integral-derivative feedback loop. In practice, for topographic imaging, this is often achieved by adjusting the integral gain just below the value where uncontrolled cantilever oscillation noise is observed in the image. Controllers may have multiple lock-in amplifiers to ensure accurate frequency-specific detection of cantilever vibration amplitude and phase. Controllers also often provide users with the ability to externally monitor AFM signals, or to supply the instrument with an external auxiliary imaging signal. Such signal access can be used to route the photodetector signal to external lock-in amplifiers with enhanced sensitivity or frequency range, or to provide customized input signals to enable new AFM modes that were not implemented at the time the microscope was manufactured.

Other common components of the AFM include an active or passive vibration isolation system and an acoustic enclosure to minimize ambient vibrations. These components are often essential to realize the x, y and z resolution limits of the instrument. Without noise and vibration isolation, lab noise and building vibration make high-resolution imaging difficult, if not impossible.

IIIb. The operating environment

One of the major advantages of the AFM compared to other high resolution microscopies is the broad range of environments within which the instrument can readily operate. Most AFMs have the capability to operate in both air and liquid immersed environments. In addition, many instruments have been operated in glove boxes with atmospheric control, in flowing liquids, and in temperature controlled systems from -35 °C to 450 °C. More customized instruments have achieved temperatures as high as 700 °C [54] and as low as a few Kelvin [55]. Furthermore some of these instruments are operated in ultra-high vacuum to achieve higher resolutions for sensitive surface characterization [55].

IIIc. Cantilever calibration

Because of the effect that forces can have on AFM results, and the requirement of accurate force measurements for many absolute property measurements, it is essential that cantilever properties and imaging conditions be accurately reported. Manufacturer-specified cantilever spring constants should be taken only as a rough guideline; more accurate measurements require user calibration of the cantilever[56, 57]. Calibration of cantilever spring constants has remained an area of intense research for over two decades. A number of viable methods to calibrate the cantilever spring constant have been proposed, each with advantages and limitations. An ideal calibration method is fast, simple, nondestructive and accurate. Below is a brief summary of some of the most common calibration methods. Other techniques exist, and more detail is provided in the mentioned references.

Thermal method – The thermal method [58, 59] has developed as perhaps the most widely used spring constant calibration method and has been integrated into many commercial instruments. The premise of the method is that a cantilever is continually vibrating as a result of Brownian motion, and the energy of that motion is proportional to the temperature. Based on the equipartition theorem, the spring constant can be determined from an analysis of the thermally vibrating cantilever's power spectral density (i.e., the cantilever's thermal vibrational energy can be related to the mechanical energy in the cantilever). The accuracy of the method generally decreases with increasing cantilever stiffness, because the magnitude of the vibration approaches the AFM noise floor. The user need only determine the sensitivity of the cantilever (i.e., the nanometers of cantilever deflection associated with a photodetector voltage) and acquire a time history of the vibration amplitude. The most significant drawback of the method is that the typical sensitivity calibration requires contacting the tip with a very rigid substrate, which can degrade the sharpness of the tip.

Reference cantilevers – In this calibration method, the uncalibrated cantilever is brought into contact to deflect a second cantilever of known spring constant [60-63]. The reference cantilever is chosen such that its spring constant is close to that expected for the unknown cantilever. In addition to the basic method of deflecting a single cantilever at a single point, two major variations have been reported in the literature. In the first, a single reference cantilever is used, but it is deflected at multiple positions along the length of the cantilever [63]. In the second method [62], an array of cantilevers of varying spring constant are alternately deflected and the unknown cantilever's response is measured. The reference cantilever technique in general has the advantage of high accuracy, but it still requires contacting a rigid material,

which can degrade the tip. It is also necessary to have a wide range of reference cantilever stiffnesses to accommodate the variety of AFM cantilevers used for various types of measurements.

Added mass – The added mass method is based on the observation that when a mass is added to the end of a cantilever beam, the resonance frequency drops in a theoretically predictable manner. To determine the spring constant of a cantilever, high density (e.g. tungsten) microspheres are placed on the end of a cantilever and held in place by adhesive forces [64]. Then, the resonance frequency of the cantilevers is measured and a model is used to calculate the spring constant. Significant benefits of the method are that calibration can be performed without having to engage a rigid sample and the spheres can be removed, making the method nondestructive. The major drawback to the method is the precision and care required to successfully add and remove the particles from the cantilever.

IV. Topographic imaging

For any AFM technique, the surface topography image will be composed of contributions from the true sample height, the local sample stiffness, and the tip geometry. The contribution of the first variable is relatively intuitive, but the contribution of the latter two variables warrants a brief additional discussion. The sample stiffness contributes to observed topography because more compliant regions of the sample will deform more than stiffer regions for the same applied load (whether quasistatic or dynamic). For precise topographic measurements of compliant materials, care should be taken to minimize the tip-sample interaction force. The tip geometry contributes to the image because the size and shape of the tip can be of similar

dimensions to surface features themselves. Thus a dilation effect occurs where protruded

features are larger than the true topography and depressions are smaller. Likewise, measured

surface radii are confounded with the end radius of the tip. Algorithms exist for correcting this
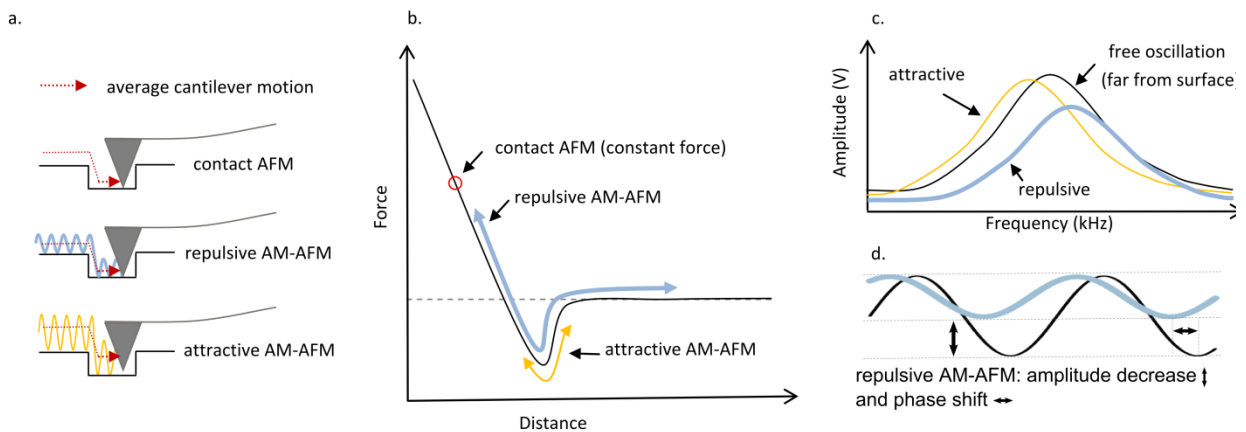
tip artifact [65].

Figure X.3. a. Topographic imaging modes include contact AFM, intermittent contact AFM (IC-

AFM) and non-contact AFM (NC-AFM). b. A model force curve demonstrating the operating

regimes of contact, IC-AFM, and NC-AFM. c. Amplitude attenuation and phase shifts in IC-

AFM and NC-AFM.

IVa. Contact mode

There are two common classes of imaging methods used to achieve topographic reconstruction

of a surface with the AFM (figure X.3.a). The first method that was developed is known as

contact mode atomic force microscopy. In contact mode the tip is moved toward the surface

until the tip makes contact with the surface and the photodetector registers a specified voltage

indicating a specific deflection of the cantilever. That voltage is directly proportional to the distance the cantilever has deflected, and the constant of proportionality is called the optical sensitivity. Conversion from deflection to force is then straightforward using one of the spring constant calibration procedures outlined above. When the cantilever reaches the requested setpoint, a feedback loop continually adjusts the z-actuator extension to maintain constant bending of the cantilever. If the tip or sample is rastered while maintaining the deflection setpoint, an image of the voltage driving the z-actuator will be proportional to the height of the surface. Contact mode is simple to operate, and is used as the foundation for other more advanced modes such as friction force microscopy [66], conducting atomic force microscopy[67] and atomic force acoustic microscopy [68]. The major limitation of contact mode is that scanning in continuous contact produces relatively large lateral or shear forces at the tip-sample contact zone.[69] For mechanically rigid and robust materials, the consequence of these forces is typically fracture and wearing of the tip, which gradually degrades resolution [70]. For compliant materials such as soft polymers and biomaterials, excessive shear forces can damage the sample [69], or even make imaging impossible. Operation with compliant cantilevers (e.g. spring constant less than 0.2 N/m) can reduce, but not eliminate, tip and sample damage. To address the limitations of contact mode, the intermittent contact modes of operation were developed.

IVb. Intermittent contact modes

As the name implies, intermittent contact modes of operation involve the periodic making and breaking of repulsive contact (or short-range attractive interaction) between the tip and

sample. This limits tip and sample damage that arise from shear forces. Intermittent contact atomic force microscopy (IC-AFM) has been a subject of intense research since its original development. A complete survey of the technique and its variants is outside the scope of this chapter, hence only the most commonly used methods are presented here. The most common form of IC-AFM is known as amplitude modulated atomic force microscopy (AM-AFM), but is also commonly referred to by the trade name "Tapping Mode" [71, 72]. The general capability to perform AM-AFM or similar variants is available on most AFM instruments. The technique typically uses relatively stiff cantilevers for operation in air (with spring constant approximately 40 N/m), whereas more compliant cantilevers (with spring constant less than 1.0 N/m) are used in liquids. In AM-AFM the cantilever is oscillated at a frequency near its resonance frequency. The oscillation is commonly produced by a dithering piezo element [71] located near the cantilever base, but excitation can also be produced by use of other methods (e.g., magnetic [73], photothermal [74, 75]). By sending the photodetector signal to a lock-in amplifier and feeding the drive oscillation as a reference, the amplitude and phase of the vibrating cantilever can be determined. When the cantilever is brought close to the surface, the vibration amplitude will be reduced due to attenuation and stiffening of the tip sample interaction. Analogous to the deflection feedback in contact mode AFM, in AM-AFM the controller will receive feedback on the oscillation amplitude and control the z-actuator to keep the oscillation amplitude constant during imaging. For many surfaces, this method maintains a stable average distance between the tip and sample, resulting in an accurate measurement of topographic heights. While the amplitude feedback provides near-constant average scanning height for the tip, the phase signal can simultaneously provide contrast related to the energy dissipation in

the sample [76, 77]. In some cases, the phase can be directly correlated with material

properties such as the viscoelastic loss tangent [78].

AM-AFM imaging can be performed at a range of setpoint amplitudes, and two distinct imaging

regimes are possible (figure X.3. a and b) [79]. At higher relative setpoints (ratios of the

setpoint amplitude to the free amplitude), the tip will interact with the sample with a net

attractive force (see the thinner light line in figure X.3.b). Imaging in this regime is often

referred to as non-contact AFM. Because repulsive interactions are minimized, sample damage

is minimized, and tip sharpness is preserved. At lower relative setpoints, the cantilever taps

harder on the surface, and net-repulsive forces dominate the tip sample interaction (see the

thicker line in figure X.3.b). This regime is often more stable than the net-attractive regime, and

provides sharper feature contrast. The two regimes can be readily differentiated by monitoring

the phase signal of the AFM (figure X.3.c). If the free cantilever vibration is setup to ensure that

the phase signal is 90 ° out of phase with the drive signal, and the cantilever is driven precisely

on resonance, the imaging phase will reveal the operating regime. If the imaging phase angle is

greater than 90 °, the cantilever is imaging with a net attractive force. If the imaging phase

angle is less than 90 °, the cantilever is imaging with a net repulsive force (in some instruments,

the relation is reversed, and this relation should be confirmed with the manufacturer). For

samples with strong chemical and mechanical heterogeneities, it is possible for both regimes to

exist within the same image, under typical imaging conditions. For the most accurate

topographic results, the user should choose a setpoint that ensures the entire image is acquired

in the same operating regime (i.e., the setpoint should be high enough or low enough so that

the image is entirely net-attractive or entirely net-repulsive).

In addition to the AM-AFM mode, another common intermittent contact mode of operation is frequency modulated atomic force microscopy (FM-AFM) [72, 80]. The method is similar to AM-AFM, but the feedback is made on the resonance frequency of the cantilever rather than on the oscillation amplitude. As the cantilever approaches the surface, the net force between the tip and sample will initially be attractive, then at smaller distances repulsive. In the attractive regime, the resonance frequency will decrease relative to that of a cantilever operating far from the surface (figure X.3.c upper, thin orange line). In the repulsive regime, the resonance frequency will increase (figure X.3.c upper, thick blue line). FM-AFM is useful because the resonant frequency shift is proportional to the average force-distance-gradient between tip and sample. The AFM controller works to ensure that the drive frequency is constantly on-resonance, regardless of how much the absolute resonance frequency shifts across the sample. FM-AFM is most commonly used in high vacuum environments instead of ambient conditions because the quality factor of the cantilever resonance is extremely high, making the measurement of resonant frequency very precise.

V. Applications of topographic imaging to membrane science

The capabilities of the AFM for high resolution surface topography imaging have been widely utilized in the membrane community. Applications include characterization of surface morphology, surface roughness, pore size and fouling.

Va. Surface roughness

Surface roughness of membrane materials has been widely studied with the AFM. Roughness has been found to correlate with permeability and fouling characteristics of the membrane, and

as such can serve as an important predictor of membrane performance. Roughness is generally

quantified by either an arithmetic mean or root mean square (RMS) type calculation [81], as

follows. An AFM topography image consists of an array of pixels at every x and y coordinate,

and each pixel contains height information for the particular location. The arithmetic mean

roughness R_a of an AFM topography image is calculated as

$$R_a = \frac{1}{n} \sum_{i=1}^{n} \left| z_i - \overline{z} \right| ,$$

and the RMS roughness R_{RMS} is calculated as

$$R_{RMS} = \left(\frac{1}{n} \sum_{i=1}^{n} \left(z_i - \overline{z} \right)^2 \right)^{1/2} ,$$

where in both cases, n is the total number of image pixels, z_i is the height value of sn individual

pixel, and $\overline{z}$ is the mean height of the entire surface. Often, some form of leveling is applied to

the flatten height image (and these tools are available in most commercial AFM software);

however, any leveling algorithms that include higher-order terms can potentially alter the

calculated roughness. Because of the tip dilation effects, the measured RMS roughness of a

surface depends on the size and shape of the AFM tip. Sedin and Rowlen [82] found that for

small scan areas, a larger tip tends to decrease the apparent surface roughness; however, for

larger scan sizes, increasing tip size will increase apparent surface roughness. Follow up

simulations by Chen and Huang[83] found that the discrepancy in roughness with tip size was

also affected by the skewedness of the height distribution. A Gaussian distribution of heights

or a surface with negatively skewed height distribution (that is, a surface where a majority of

the pixels have height values below the mean value) will result in R_{RMS} values that decrease with increasing tip radius. In contrast, when the height distribution is positively skewed, roughness will initially increase, then turn and decrease with increasing tip size. These geometric effects on surface roughness can be understood by considering the ability of a tip of given radius to fully penetrate a valley of given dimension. A large radius tip cannot penetrate a narrow valley, resulting in a lower measured roughness. The decrease in measured roughness with high positive skewedness results from coupling of the tip shape into the profile of peaks on the sample. This broadens those peaks, and reduces measured roughness.

Boussu and coworkers [14] showed that the absolute determination of roughness was also affected by the AFM imaging mode used. Repulsive-regime AM-AFM and non-contact (i.e., attractive-regime) AM-AFM gave roughness values on the same membranes, with the same scan size, that differed by up to 100 %. There was not a clear bias direction between the two modes, with either technique showing higher roughness under certain conditions. The difference in measured roughness with different AFM modes was attributed to the ability of non-contact AFM to image on top of a contamination layer such as surface-water, whereas repulsive regime AM-AFM would tend to penetrate this contamination layer and image the underlying material. In spite of the absolute differences, the rank order of all membranes remained the same for both imaging modes.

Overall, the calculated roughness will depend on imaging mode, tip size, and scan size. This indicates that caution must be used in the reporting of absolute roughness results.

Furthermore, roughness comparisons between surfaces are most valid when tip and imaging conditions are kept as constant as possible.

Many studies have reported on the roughness parameters of membrane materials; however, fewer have sought to quantitatively and systematically correlate membrane performance with surface roughness. Examples from the literature are discussed below.

In an early study Hirose and coworkers [84] prepared a series of model polyamide reverse osmosis (RO) membranes in which the roughness was varied by addition of isopropyl alcohol. The resultant membranes had R_{RMS} values ranging from 21 nm to 105 nm. As shown in figure X.4, a roughly linear correlation was found between surface roughness and membrane flux. It was proposed that increased surface roughness increases the surface exposed to upstream fluid, while not detrimentally increasing the average thickness of the membrane.

Madaeini [13] examined the effects of surface roughness on the flux and ion retention of RO membranes. The author compared two membranes, TFC-ULP and TFC-SR2 (both from Fluid Systems), which have similar polyvinyl alcohol chemical structure in the skin layer, but exhibit dramatically different flux and ion retention. TFC-ULP exhibited low water flux and high ion retention, whereas TFC-SR2 exhibited high water flux and low retention. Following IC-AFM imaging of the surfaces, the author found that TFC-ULP exhibited significantly higher surface roughness than TFC-SR2 (more than 100x increase in R_{RMS}). The rougher surface could trap more ion species, which resulted in increased retention and decreased flux. The seeming contradiction with the work of Hirose[84] may arise from less control over skin thickness in the Madaeini study.

Al-Jeshi and Neville further studied the effects of roughness on RO membrane performance

[15]. They characterized 4 commercial RO membranes with nominally similar chemical

composition. Roughness varied from 17 nm to 70 nm between the membranes, with 10 % to

15 % standard deviation amongst different regions of the same membrane. In contrast to the

earlier findings, a clear monotonic correlation between flux and roughness was not observed.

In the most extreme example, Osmonics AG and Osmonics AD membranes had surface

roughness values within 1 nm of one another; however, their flux differed by a factor of more

than 7. This result indicates that although surface roughness can strongly influence flux,

additional chemical and structural characteristics of the membranes can still dominate.

Another key finding was that RMS surface roughness changed considerably ($\approx$ 35 % increase in

2 hours) after exposing a dry membrane to water. This indicates that relevant surface

roughness measurements should be performed in the operating environment, rather than in
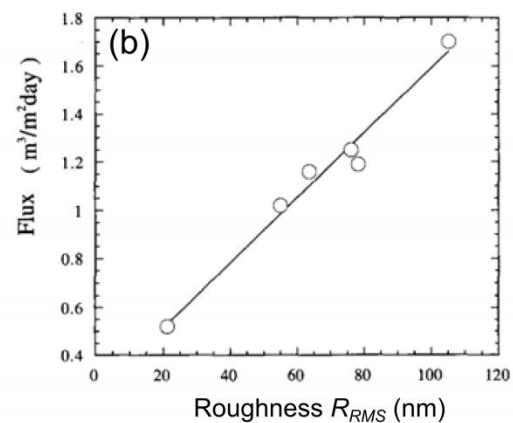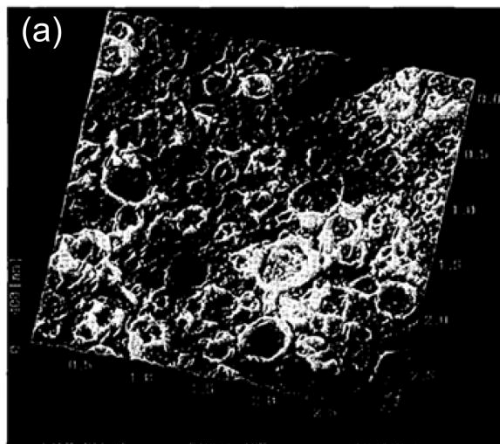
ambient conditions.

Figure X.4: (a) Example topography image of a reverse osmosis membrane and (b) plot showing the linear correlation between AFM-derived, nanometer-scale surface roughness and bulk membrane flux for a series of 6 RO membranes. From [84]

In addition to influencing the flux of pristine membranes, roughness has also been shown to affect the tendency of membranes to foul. In a comparison of relatively smooth cellulose acetate membranes and rough polyamide composite membranes, exposure to a silica colloid suspension led to much faster flux decline in the rougher composite membranes [10]. In a follow up study [12], Hoek et al. studied roughness and fouling on 4 different membranes: two nanofiltration membranes and two RO membranes. Membranes were tested with a 200 mg/L suspension of 140 nm silica particles as a model foulant.   They found a direct monotonic correlation between percent flux decline and surface roughness, independent of the membrane type. Flux decline was proposed to be more severe for the rough membranes because the particles could clog the valley-like features present. Appreciable flux decline on smooth membranes required a nearly continuous cake layer of particles to be formed, and that layer must be tens of particle diameters thick. Post-fouling topographic scans confirmed the nature of the proposed clogging mechanisms for smooth and rough example membranes.

A study by Hobbs et al. [16] utilized high-organic-content surficial groundwater instead of model colloidal solutions. Again, RO and NF membranes were compared on the basis of surface topography and flux decline during filtration. A total of six RO or NF membranes were characterized. As shown in figure X.5.a, for the RO membranes, the authors observed the same

trend as prior authors wherein the flux decline increased with increasing surface roughness.

For the NF membranes in figure X.5.b, the trend was weaker and showed a slight trend reversal, with reduced flux decline at increased surface roughness. The discrepancy was rectified when instead of surface roughness, the authors considered the surface area difference (i.e., the ratio of 3-dimensional surface area to specified scan area) of the membranes, as shown in figure X.5c-d. The improved correlation between flux decline and surface area difference is attributed to the ability of the increased surface area difference calculation to quantify the total surface area available for adsorption.
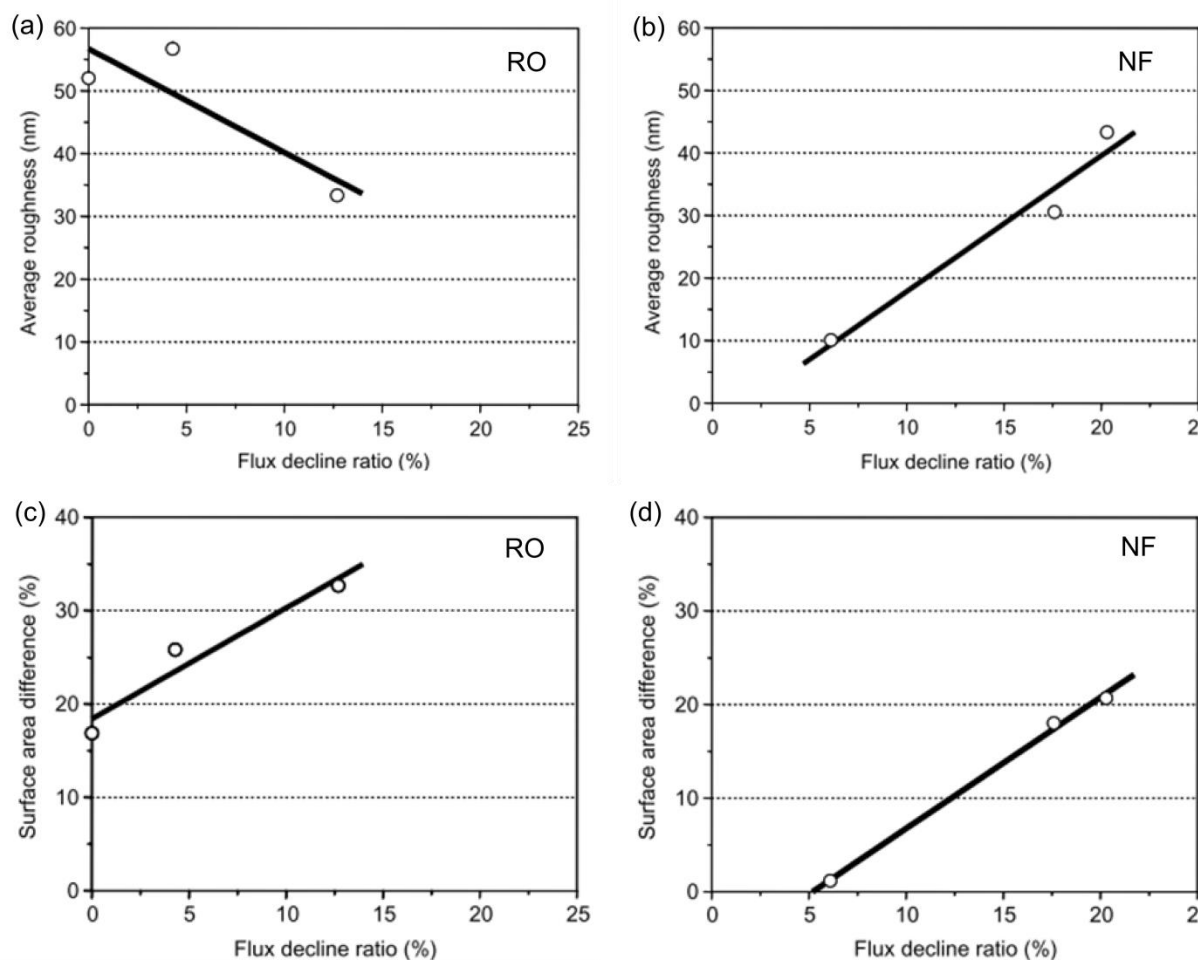
Figure X.5: (a) and (b) Plots showing the correlation between AFM-measured surface roughness and fouling induced flux decline ratio for RO and NF membranes, respectively. (c) and (d) show the correlation between AFM-measured percentage surface area difference (defined by the ratio of 3-dimensional surface area to flat projected image area) and flux decline ration for RO and NF membranes, respectively. From [16]

In a more recent study, An et al. [85] studied the influence of polyvinyl alcohol on surface morphology and antifouling characteristics of composite polyamide NF membranes. Varying the mass fraction of polyvinyl alcohol from 0 % to 16 % resulted in a decrease in RMS roughness

from $R_{RMS} \approx 110$ nm to $R_{RMS} \approx 40$ nm. These changes were accompanied by up to 20 % reduction in flux decline; however, the modifications came at the expense of a significantly reduced rejection rate towards $MgSO_4$, NaCl and methyl orange. The less rough surfaces also exhibited higher total flux due to the increased affinity between the feed solution and the more hydrophilic membrane.

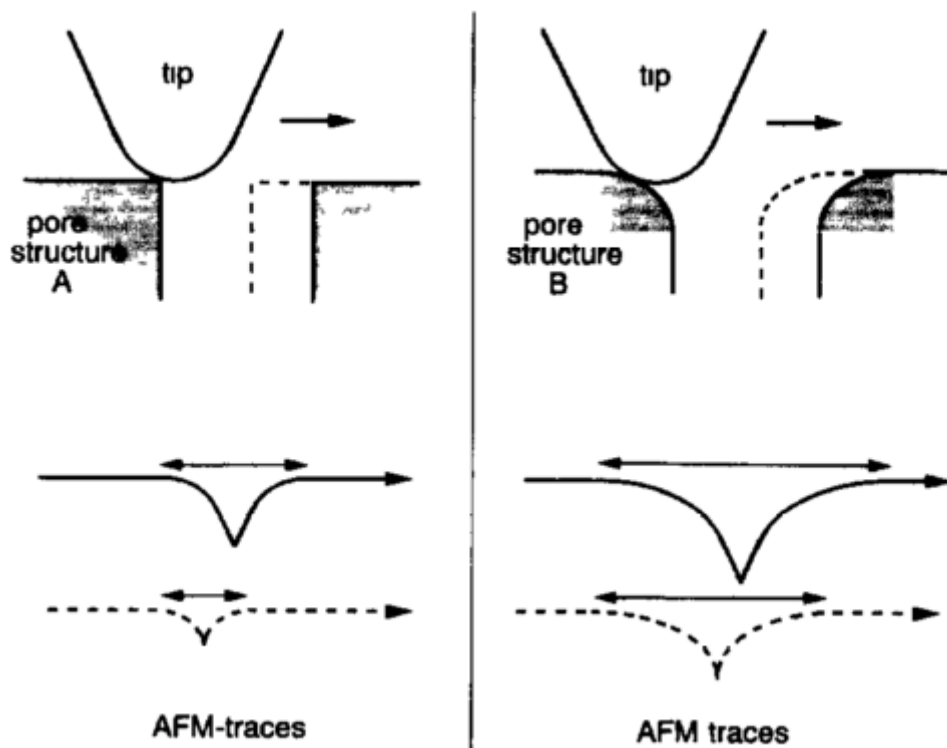### Vb. Pore size determination

Figure X.6. The impact of tip shape (relative to the pore) on the AFM topography images of membrane pores for two different pore shapes (structure A and structure B) and two different pore sizes (solid line and dashed-line). The pore size can be determined for the pore

shape in structure A, but cannot be accurately determined for the pore shape in structure B.

From [86]

The high resolution of the AFM makes it an attractive tool for characterizing the nanoscale pore structure of many filtration membranes. The fact that AFM probes only the surface morphology of the pores and can provide little information about the deeper structure must be considered when performing a pore size analysis (figure X.6). Further, the AFM tip can only probe a pore up to the depth where the pore diameter is comparable to the cross-sectional diameter of the tip. Thus, pores will appear as rounded valleys rather than straight-sided holes. In spite of the limitations imposed by the finite tip size and surface specificity, considerable progress has been made in imaging pores. The AFM was first used to characterize membrane pores by Dietz et al. in 1991 [87]. They compared three different membranes with two polymers and two molecular weight cutoff values. For two membranes with similar polysulfone composition, there was a clear correspondence between pore density and molecular weight cut-off. Pore sizes in the range of 15 nm to 30 nm were observed; however, this was still larger than expected from the molecular weight cutoff. Reasons for the discrepancy were not thoroughly investigated.

Fritzsche et al. [88] compared the pore size measuring capabilities of the scanning electron microscope (SEM) and AFM on 10,000, 30,000 and 100,000 molecular weight cutoff (MWCO) ultrafiltration membranes. Pore size was determined from a line cross section of the topography image by measuring the size of prominent valleys. For the 10,000 MWCO

membrane, neither SEM nor AFM could adequately resolve the individual pores, which were expected to be between 3 nm and 5 nm in diameter. It was hypothesized, and substantiated with flux measurements, that the solvent exchange required to prepare the SEM specimens resulted in closure of the pores. For the AFM specimens, the micromachined probe tips available at the time lacked the sharpness for probing such pores. For the 30,000 MWCO and 100,000 MWCO membranes, both AFM and SEM could resolve the pore structure; however, there was considerable discrepancy between the measured diameters. The AFM measured pore diameters were consistent with expectations from the MWCO value, whereas the SEM measured much smaller average pore diameters. Similar to the 10,000 MWCO membrane, flux testing indicated partial closure of the pores when membranes were prepared for SEM. The easy and nondestructive sample preparation and environmental capabilities of AFM are thus a significant benefit for pore size measurements.

Bowen et al. performed extensive studies on the AFM characterization of membrane pores. In 1996 [22], the group evaluated the use of noncontact AFM for characterizing pore size and pore size distribution. The cantilever had a high aspect ratio tip with an end radius of $\approx$ 10 nm. Pore sizes were found to be comparable to those from contact-mode AFM, but they again differed considerably from sizes measured with electron microscopy. The ability to use noncontact AFM to characterize pores provides significant opportunity for the characterization of delicate membrane surfaces that would otherwise be damaged by higher normal or shear forces, or strong electron beams. In a related study [21], the authors found that the highest pore resolution was possible on very smooth membranes where local peaks and valleys did not obscure the pore structure.

To improve the ability to characterize pore size, Bowen et al. investigated the use of Fast

Fourier Transform (FFT) to process images of the membrane surface [89]. A review of the

literature by the authors found that AFM imaging often resulted in an apparent elongated pore

structure that was not verifiable by complementary techniques. The authors found that, for a

model microfiltration membrane, such elongation arose because of cantilever vibrations from

fast scan rates and the use of low-spring-constant cantilevers. As shown in figure X.7,

application of an FFT to the raw data, radial filtering of high spatial frequencies, and inverse FFT

of the processed data resulted in much more circular pores that were consistent with

expectations. Another paper by Bowen and colleagues [24] summarized the state of the art at

the time of publication in 2000. They observed that the sometimes limited correspondence

between AFM-measured pore size and MWCO data as previously reported by other groups was

a result of not operating with the most sophisticated equipment and analysis. The use of FFT

image processing, in addition to high aspect ratio tips (rather than low aspect ratio pyramidal

tips), provided the best agreement with MWCO predictions. This agreement was best for

smaller pore diameters, and for samples with a small standard deviation in pore size.

Stawikowska and Livingston [28] recently took the use of a high aspect ratio tip to an extreme

case where the tip was a carbon nanotube ~2 nm in diameter. Although their theoretical

spatial resolution was much higher than for previous studies with sharpened silicon or silicon-

nitride tips, they were cautious about misinterpreting the surface roughness of the film as

evidence of nanoscale pores. The membranes under investigation were expected to have sub-

nanometer pore sizes, but the sharp probe revealed evidence of 1.5 nm to 2.1 nm pores. In

fact, characterization of a dense film that was found to have no measurable flux still resulted in

a calculated 3.5 nm pore size using the conventional approach from the literature. Thus, to

confidently identify and measure pores requires not just a very sharp tip, but also pores that

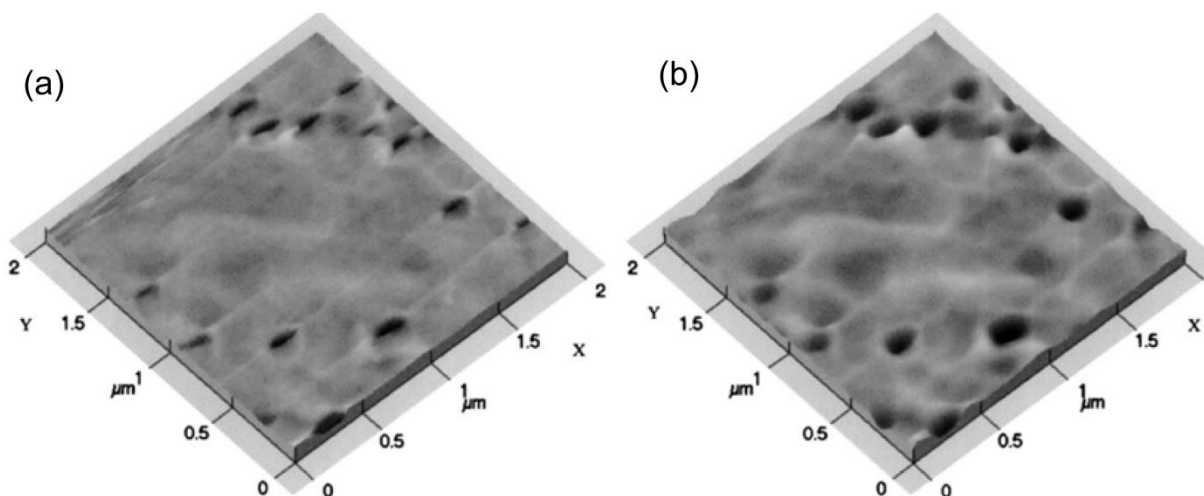are large or otherwise discernible from the background roughness.

Figure X.7: (a) Raw AFM image of surface and pores of a C01 cyclopore membrane in air. (b)

The same image after post-processing with a fast Fourier transform (FFT) to remove transient

vibrational noise. From [89]

VI. Spectroscopy and functional imaging

The spectroscopic capabilities of the AFM were recognized early in the development of the

instrument. In general, spectroscopic data are acquired at a user-defined location on the

sample, and a dependent variable is adjusted while monitoring the response of some

independent variable. Common measured data pairs include of force versus distance, voltage

versus distance, and current versus voltage. Functional imaging refers to either spectroscopic

data obtained at an evenly-spaced array of points to show spatial variation of specimen

properties, or spectroscopic data captured in parallel with traditional scanning modes.

VIa. Force-Distance Spectroscopy

One of the first developed and most widely used forms of AFM spectroscopy is force-distance

(F-D) spectroscopy. In force-distance spectroscopy, the base of the cantilever is brought

towards the sample at a constant velocity. After some threshold is reached (usually base

displacement or cantilever deflection), the direction of motion is reversed and the cantilever is

withdrawn. Although a simple experiment, F-D spectroscopy can provide rich information

about the mechanical and chemical properties of the surface. An example F-D spectroscopy

curve is shown in figure X.8. As the cantilever approaches the surface, it is initially subjected to

only weak long range forces (e.g. electrostatic). This can cause some deflection of the

cantilever; however, the extent of this deflection is usually small. At some critical tip-sample

distance, the attractive force gradient between the tip and sample exceeds that of the

cantilever spring constant, causing the tip to snap into repulsive contact with the sample.

Further advancing of the cantilever toward the sample results in a repulsive bending of the

cantilever, and increased deflection. In this repulsive regime, the slope of the force versus

displacement curve is proportional to the vertical stiffness of the sample (known as the contact

stiffness). During the cantilever retraction, the slope may precisely trace the approach curve, or

if a dissipative process such as plastic deformation has occurred, the slope may be altered. The

most significant difference between the approach and retract curves occurs in the regime of

negative deflection or voltage relative to that of the lever far from the surface. During

retraction, adhesion forces (e.g. electrostatic, capillary, Van der Waals) between the tip and

sample cause the tip to remain in contact until the pulling force exceeds the adhesion force. By

measuring the magnitude of this dip relative to the free cantilever baseline and choosing a

suitable analysis model, the adhesive properties of a surface can be characterized.

Particular problems that have been addressed by F-D spectroscopy include local mechanical

property characterization, chemical mapping with functionalized probe tips, and single

molecule spectroscopy. Each of these measurements has applications in membrane science,
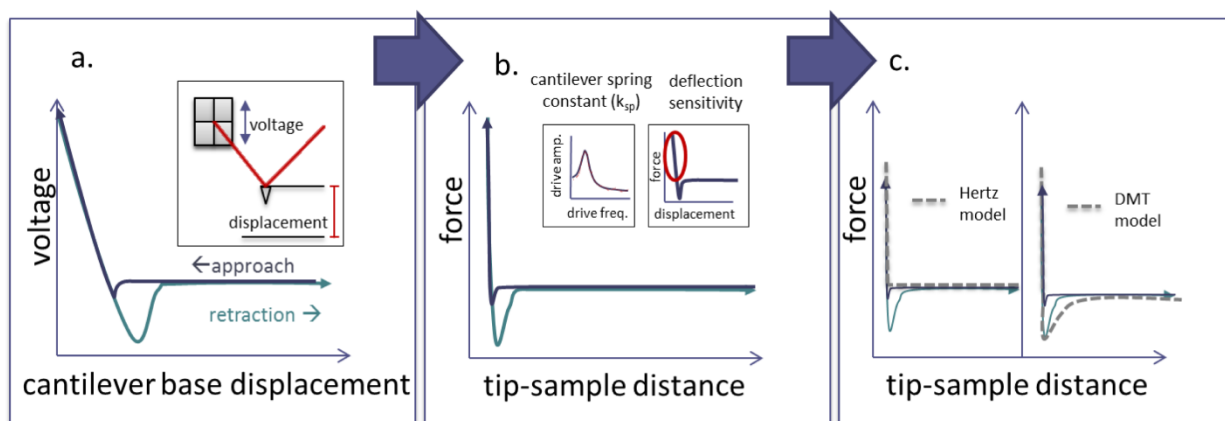
and each measurement is discussed below.

Figure X.8. The extraction of quantitative mechanical properties from F-D spectroscopy. (a) A raw force curve for voltage versus base displacement. (b) The voltage versus displacement curve is converted to a force-versus-distance curve using the deflection sensitivity and the cantilever spring constant obtained from a thermal spectrum or another calibration method. c) Quantitative mechanical properties can be extracted by fitting the F-D curve with a contact mechanics model.

VIb. Contact mechanics models

The extraction of quantitative mechanical properties from F-D spectroscopy relies on principles from the field of contact mechanics, and is similar to instrumented indentation. Thus, it is necessary to convert the uncalibrated cantilever F-D spectroscopy signals from units of voltage versus cantilever-base displacement to units of force versus indentation depth (figures X.8 a and b). The tip sample distance, D is given by

$$D = Z_P + Z_L + \delta,$$

where Z_P is the cantilever base piezo displacement, Z_L is the cantilever tip displacement, and δ is the indentation depth that the tip has pushed into the sample (minus the amount the tip itself has deformed). Z_P is known from the calibration constant between piezo voltage and sample height. Z_L is typically given in volts, but can be calibrated to a distance from an F-D measurement on a very stiff reference material (the calibration constant is the lever sensitivity in units of nm/V). In the repulsive regime of an F-D curve on a very stiff sample, $\delta=0$ and $D = 0$, making determination of Z_L straightforward. For a polymeric membrane material or other compliant sample, a F-D curve on the adjacent stainless steel puck or glass slide to which the membrane is adhered is generally sufficient. The lever sensitivity will remain constant as long as the reflected laser position on the cantilever does not change. Thus, a subsequent F-D measurement on a compliant test material will have only one unknown, δ. The dependent force variable is calculated by the product of Z_L and the cantilever spring constant.

To extract the mechanical properties including stiffness and adhesion, the force versus indentation curve must be fitted to a contact mechanics model (figure X.8.c). Typical models for the calculation of elastic properties of materials from force curves between a hemispherical tip

and a flat surface are Hertzian [7], Derjaguin-Müller-Toporov (DMT) [90], and Johnson-Kendall-

Roberts (JKR) [91]. The Hertz model is the classical theory of contact mechanics, which assumes

that there are no adhesive interactions between the tip and the sample, the deformation

caused by tip-sample contact is entirely elastic, and the contact area is much smaller than the

tip radius. Assuming the tip is much stiffer than the sample, the Young's modulus E of the

material can be extracted from a fit of the F-D curve using the following equations depending

on the shape of the tip:

Spherical Tip

$$F = 4\frac{\sqrt{R_C}}{3}\frac{E}{1-v^2}\delta^{\frac{3}{2}},$$

where F is the applied force obtained from the F-D curve, R_C is the radius of tip curvature, and v

is the Poisson ratio which must be estimated for the material of interest.

Conical Tip

$$F = \frac{E}{1-v^2}\frac{2\tan\alpha}{\pi}\delta^2,$$

where α is the half opening angle of the cone.

The F-D curve is generally fit with a model making the Young's modulus E an adjustable

parameter. Successful quantification of the Young's modulus therefore depends on accurate

knowledge of tip shape and size as well as a reasonable estimate of the Poisson's ratio for the

material of interest, which can generally be estimated from the bulk material properties.

The DMT and JKR models additionally incorporate adhesive interactions, with DMT being used for low adhesive forces relative to the material elasticity and JKR being most appropriate for high adhesive forces relative to the material elasticity. The JKR model is a fully elastic model that also considers adhesive interactions in the contact area, and the DMT model adds both adhesive and Van der Waals forces outside the contact area to the Hertzian contact model. The development of these two models is outside of the scope of this chapter and is treated in detail in the following references [7, 90, 91]. All three of these models are for small indentations into the material (i.e., indentation significantly smaller than the tip radius). With either method, indentations must be small enough that the underlying material does not influence the measured mechanical properties. For larger indentations that cause plastic deformation of the contact, other models (e.g., Oliver-Pharr [92]) should be considered.

VII. Applications of force spectroscopy to membrane science

Obtaining the mechanical properties of membranes is important for handling, assembly, and lifetime estimation purposes, depending on the specific membrane application. Additionally, changes in membrane properties after harsh chemical treatments can be studied by AFM to determine the susceptibility of certain membrane materials to different treatments. The local environment of polymeric membrane materials can influence the swelling of polymer chains, which can translate into a local stiffness change. One of the largest challenges to membrane-based water treatment is colloidal fouling (whether inorganic, organic, or biological). The AFM offers a unique platform to directly measure the interaction forces (specifically adhesion forces) of individual colloids with membranes. Stiffness and adhesion measurements on polymer films

are a fairly routine AFM experiment. Advantages of measuring these properties by atomic force

microscopy instead of macroscopic methods are the high spatial resolution for probing

mechanical properties on the micrometer and submicrometer scale, and the high sensitivity to

small forces. There are also some disadvantages and challenges to extracting membrane

mechanical properties by use of F-D spectroscopy. The tip radius must be known and smoother

surfaces than most membranes are required, as all of the models to extract mechanical

properties are highly dependent on the tip-sample contact area. Similarly, small asperities in

the tip or membrane can lead to the underestimation of adhesion forces. However, with the

right experimental considerations F-D spectroscopy is a promising tool, particularly for

understanding micrometer and submicrometer heterogeneities in stiffness and adhesion of

membrane materials.

VIIa. Mechanical property measurements

Only a handful of studies have attempted spatially resolved stiffness measurements on

polymeric membrane materials. One reason for the small number of stiffness studies may be

the inherent difficulty of performing these measurements on rough surfaces, which are notably

present on many membranes. As mentioned above, in order to extract quantitative mechanical

properties from AFM force data, detailed information about the cantilever and the material

properties must be known, including the tip radius, the cantilever spring constant and the

Poisson's ratio of the material. Nanomechanical measurements of contact stiffness by AFM are

more challenging to obtain than bulk material measurements, but can be particularly valuable

when spatial information (i.e., for polymer blends or composite materials) is needed. The most

promising applications are for thin films (which are not conducive to macroscale testing), for studying the local effect of polymer/environment interactions and for characterization of the heterogeneity of composite membrane materials.

As an example of membrane-environment interaction measurements, Umemura and colleagues [46] used an AFM to measure the Young's modulus of Nafion in air, water and mixtures of water and methanol. The authors measured a series of force curves and used the Hertz contact model to extract values for the Young's modulus. It is important to keep in mind that the Hertz contact model neglects adhesive forces, and polymer samples must be significantly thicker than the indentation depth to ensure that the tip geometry matches the indentation shape, and to remove the effects of the underlying substrate on the measurement. The Young's modulus (measured using the same cantilever on the same membrane) decreased by a factor of 1.75 when switching from water to 5 % methanol, which the authors attributed to swelling of the polymer chains in the Nafion thin film. The measured modulus remained constant when switching from methanol back to water, which suggests a high affinity of the polymer for methanol.

Another example where the AFM excels for modulus measurements is characterizing the heterogeneity of composite membrane materials. The nanomechanical properties of poly(vinyl alcohol) (PVOH)–poly(acrylic acid) (PAA)–cellulose nanocrystal (CNC) membranes were measured using AFM nanoindentation experiments [45]. Once again, the Hertz contact model was used to extract the Young's modulus, and the cantilever was chosen to have a high spring constant (nominally 311 N/m) so that applied forces were relatively large and adhesive forces

could be neglected. The authors found that the modulus determined with AFM showed good relative agreement with modulus determined from bulk testing when the ratio of PVOH:PAA:CNC was varied. However, the AFM measurement overpredicted absolute modulus values by a factor of 1 to 2. The largest discrepancy between AFM and bulk testing occurred for samples where the CNCs exhibited substantial agglomeration.

A relatively new mode that combines intermittent contact topography imaging with the generation of a force curve at each pixel (trade named PeakForce Tapping) has been used to map nanomechanical properties at the nanoscale for a variety of polymer materials [47]. The force curves are fit using the DMT model (Hertz plus adhesion forces). Heisgen et al. [43] used PeakForce mode to map the stiffness and adhesion of Nafion membranes before and after they had been "activated" by applying a current through the material. The authors found that the areas around pore openings were the least deformable, and that areas with decreases in adhesion corresponded to the swelling of bumps on the polymer membrane. The bumps were attributed to water pressure, and the decreased adhesion was suggested to be caused by a decrease in the fraction of Nafion polymer backbones at the surface. The adhesion force was calibrated using a set of materials with different polytetrafluoroethylene (PTFE) content. The authors were able to use the data to correlate the observed results to a model structure containing bundles of fibrils.

Heisgan et al. also investigated the properties of gas diffusion layers for fuel cells and used the relative change of energy dissipation and adhesion force as a measure of PTFE content to observe the aging of fuel cell layers [44]. The authors used another intermittent contact mode

method (trade name HarmoniX) that extracts a force curve at every pixel by analyzing many harmonic signals at each point in the intermittent contact mode cycle and monitoring the torsional bending of special asymmetric cantilevers. They were able to correlate the local power losses to the distribution of material degradation in the micro porous electrode.

VIIb. Adhesion measurements

A more common use of F-D spectroscopy in membrane science is to understand how fouling components interact with membrane surfaces [7, 93, 94]. The adhesive force is determined from the retraction portion of the force curve. Because of the challenges with determining tip size and shape (often this must be done by electron microscopy on the exact same cantilever used for measurements) many of these measurements are performed with a colloidal probe modified cantilever that is easier to characterize [93]. Colloidal probe cantilevers can be purchased from a few manufacturers, or the probes can be assembled in the lab using epoxy to attach polymer or silica microspheres to the end of the cantilever. The most common probe for membrane studies is a carboxyl-modified latex microsphere, which researchers have postulated mimics the carboxyl groups on model foulants such as humic materials or cell surfaces [93, 95]. A summary of specific applications of adhesion measurements follows.

Bowen et al. were the first group to quantify the interaction forces of individual colloids with water treatment membranes using atomic force microscopy [38]. The group modified a tipless, relatively compliant (cantilever spring constant of 0.4 N/m) silicon nitride cantilever with an 11 mm polystyrene microsphere. Force curves were obtained for the polystyrene microsphere

with two different membrane materials: a polyethersulfone membrane and a proprietary

antifouling membrane. The adhesion force was estimated by quantifying the depth of the well

in the retraction curve and quantifying the pull-off force normalized by the microsphere radius.

The group showed that the proprietary membrane had a significantly smaller force of adhesion.

In a follow up study the adhesion of biomolecules to two different membrane materials was

quantified [39]. The test setups utilized adsorption of bovine serum albumin on to a 5-μm-

silica-colloidal-probe-modified cantilever and a single yeast cell attached to a tipless cantilever.

They were able to demonstrate smaller adhesive forces between the biomolecules and the

membrane that was most fouling-resistant in field tests; however, their measurements had

fairly large error bars, which they attributed to heterogeneities in roughness of the membrane

surface.

Even for colloidal probe measurements, membrane roughness can be an issue for adhesion

measurements. Shortly after demonstrating the first force curves between single particles and

membrane materials, the same group modified a tipless cantilever with a silica microsphere

and demonstrated the impact of a variety of different ionic strengths on the adhesion force

between the colloidal probes and rough membrane materials [11]. In both the peaks and the

valleys of the surface, the adhesion force increased with ionic strength. They also measured

significantly higher adhesion forces in the valleys than at the peaks, presumably because of

increased contact area. This artifact can be avoided by choosing a colloidal probe that is

significantly larger than the roughness of the membrane.

Brant and colleagues studied a variety of different colloidal probe materials for the colloidal probe microscopy technique on water treatment membranes [96]. They compared their results with the extended Derjaguin-Landau-Verwey-Overbeek theory (XDLVO). The group studied two different reverse osmosis membrane materials, a heat-treated cellulose triacetate/diacetate blend membrane and a thin-film composite membrane. Both membranes were relatively smooth in comparison to the colloids selected (5 μm silica, 25 μm alumina, and 5 μm polystyrene microspheres). They found that XDLVO theory, which incorporates acid base short range interactions into DLVO theory, predicted the order of adhesion forces measured between all membrane colloid pairs, particularly for hydrophilic pairs. In a follow up study [40], the authors explained these results by considering the density of the electron donor and acceptor groups on the colloid surface. These partial positive and negative sites on a hydrophilic colloid (silica) influence the hydrogen bonding with the surface, leading to higher adhesion forces than materials without such sites (polystyrene). This result was counterintuitive and could not be described by DLVO or hydrophobicity alone. The authors compared flux measurements for three commercially available reverse osmosis and nanofiltration membranes. In addition to characterizing the adhesion force by the depth of the well in the retraction curve normalized by the radius of the colloidal probe, the authors compared the results to the values of the work of adhesion calculated with the JKR model. They discovered qualitative agreement between AFM measurements and purely theoretical calculations, but the forces measured by AFM were much smaller than predicted by JKR theory. Surface roughness was attributed as a cause of the discrepancy, and the discrepancy was reduced when the JKR model was modified to account for the reduced contact area on a rougher material.
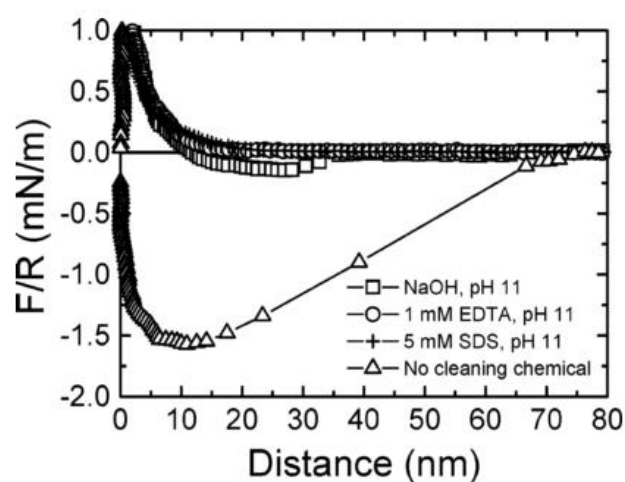
Figure X.9. Cleaning-agent-induced reduction in the adhesion force between a carboxylate-modified latex probe and fouled membranes in the presence of calcium and humic acid. From [95]

Li and Elimelech [95] performed an AFM study to elucidate the mechanism of organic fouling and chemical cleaning. They chose a carboxylate modified latex colloidal probe (4 μm diameter) as a surrogate for humic acid and studied the interactions between bare and fouled membrane surfaces in the presence of various ions and cleaning agents. They were able to demonstrate a correlation between the adhesion forces under various conditions and membrane performance; specifically, they found much higher adhesion forces in the presence of calcium ions, which was postulated to be caused by the formation of calcium bridges. They also demonstrated reduced adhesion forces in the presence of chemical cleaning agents including sodium dodecyl sulfate and sodium hydroxide and in the presence of a chelator (figure X.9).

Frank and Belfort [97] demonstrated the impact of ionic strength on the adhesion of

extracellular polymeric substance (EPS) from *Pseudomonas atlantica* to membrane materials.

They modified the surface of a colloidal probe with the EPS purified from cultures and were

able to qualitatively reproduce fouling results from the membrane community at a variety of

ionic strengths. They also found that the EPS chains collapsed at high ionic strength, leading to

indistinguishable adhesion behavior on three different membrane materials. This explains the

persistence of marine biofilms in fouling of membranes because at high ionic strength the

underlying material no longer influences adhesion.

Adhesive measurements have also been used to characterize local variations in hydrophobicity

of membrane surfaces. Using an octadecyl trichlorosilane (OTS) modified cantilever, Yamazaki

and colleagues probed the adhesive forces with a series of force curves on a wet dialysis

membrane [98]. To mitigate concerns about the influence of tip contact area, they normalized

the adhesive force between the tip and the membrane by the adhesive force of the same

cantilever on hydrophobic mica to obtain a parameter defining the intensity of hydrophobicity.

By performing F-D spectroscopy on an evenly-spaced array of points across the inside surface of

the membrane, they could quantify the strength and uniformity of hydrophobic and hydrophilic

sites. They were able to demonstrate that introduction of polyvinyl pyrrolidone (PVP) to the

membrane resulted in decreased relative intensity of hydrophobicity for two membrane types.

The addition of PVP further lead a tighter distribution of intensity of hydrophobicity for one

membrane polymer, whereas the other polymer showed little change in the width of the

distribution.

VIII. Other advanced AFM modes and their applications

In addition to the AFM techniques already mentioned, a number of other AFM and scanning probe microscope (SPM) techniques exist. Some of these have already seen use in membrane characterization, whereas others are potentially useful, but have not yet been applied. These techniques are generally extensions of the conventional AFM modes (e.g. topographic imaging, force spectroscopy) with modifications to provide new information, but in some cases they represent entirely independent instruments.

VIIIa. Electrical AFM methods

Numerous researchers have sought to characterize the electrical properties of materials using AFMs [6]. By employing a conductive coating or solid conductive material as the cantilever and tip, it is possible to operate the AFM in a number of electrical characterization modes. Some of the specific properties that can be measured include local conductivity with conductive AFM (CAFM), capacitance with scanning capacitance microscopy (SCM), surface potential with scanning Kelvin force microscopy (SKFM), impedance with scanning impedance microscopy (SIM), and piezoelectric response with piezo force microscopy (PFM). The detection of these properties can arise from direct measurement of the electrical signal or from cantilever deflection induced by an electrical force on the tip.

CAFM [67] and SCM [99] are electrical AFM methods that utilized direct measurement of an electrical signal. In CAFM, the microscope is operated in contact mode while a constant voltage is applied between the tip and sample. The current flow is typically amplified, then fed into the AFM as an auxiliary imaging channel. Depending on the insulating/conducting properties of the

surface, the detected currents can be either tunneling or ohmic. Similarly, in SCM a capacitance

sensor is attached to the cantilever, and its signal is used as the auxiliary channel for contact

mode operation. SCM can be performed with either an AC or DC bias voltage between tip and

sample.

SKFM [100] and SIM [101] are electrical AFM methods in which the electrical stimulus produces

an electrostatic force on the cantilever. The electrostatic force F_{ES} is given by

$$F_{ES} = \frac{1}{2}(\Delta V)^2 \frac{\partial C}{\partial z} \ ,$$

where ΔV is the potential difference between the tip and the surface, C is the capacitance, and

z is the tip-sample separation distance. In SKFM, an external bias applied to the cantilever is

used to cancel out the surface potential ΔV between the tip and sample. For absolute

quantification of surface potential or work function, SKFM is typically used with a double pass

mode of scanning. On the first pass, the AFM acquires the height information of the surface

(usually with tapping mode, but sometimes with contact mode); then in the second pass, the

probe retraces the surface topography at some user-defined lift-off height. During the second

(lift) pass, a feedback loop adjusts the DC bias voltage to continually cancel out the surface

potential. This DC bias voltage is then used as the auxiliary imaging channel. In SIM, the

voltage is applied across the sample instead of the tip, and the frequency is varied to explore

the surface potential's frequency dependence.

In PFM [102], an AC electrical drive signal is applied directly to a piezoelectric sample. This

creates a periodic strain in the material that is detectable by a lock-in amplifier on the

photodetector signal (referenced to the electrical drive frequency), with the AFM cantilever operating in contact mode. If local variations in material polarizability exist, they will be detected as variations in the amplitude of the AC cantilever deflection. Generally, drive frequencies are kept well below the resonance frequency of the cantilever in contact (which is higher than the free-space resonance frequency). If the AC electrical drive frequency is matched to the resonant frequency of the cantilever in contact with the sample, oscillation amplitude is increased and gains in sensitivity can be obtained; however, this comes at the expense of ease of interpretation.

Electrical AFM methods have beed widely used in the characterization of fuel cell membranes. O'Hayre et al. used a Nafion membrane as a model system to demonstrate SIM [103]. A platinum coated tip was placed in contact with an electrolyte membrane while a bias voltage drove a reaction between protons and oxygen to form water. The authors combined the SIM measurement with nanomechanical property measurements to predict the contact area between tip and the sample. This enabled an absolute measurement of electrical impedance to be performed. Values for transfer coefficient and exchange current density were both found to be in agreement with bulk measurements of the material. Kanamura et al. applied SKFM (called surface potential microscopy in the article) to distinguish ion channels in dry and hydrated Nafion® membranes [104]. It was found that the ion channels were significantly broadened in the hydrated membrane, exemplifying the dynamic nature of the membrane morphology.   Boussian et al. used CAFM to further investigate the conducting channels in Nafion [105], this time with an active proton fuel source.   The CAFM image was found to be uncorrelated with a simultaneously acquired topography image. The results further indicate

that only a limited number of ion channels penetrate the entire thickness of the membrane, and many of those channels may not be in direct contact with a catalyst particle on the underside. Xie et al. also used CAFM to measure the spatial and humidity-dependent variability in ion conduction [106]. Histogram analysis of the CAFM images revealed that both the peak value of the current and the width of the current distribution increased with increasing humidity. CAFM has also proven useful for characterization of novel block copolymer fuel cell membranes. Takimoto et al. used CAFM (which they called electrochemical atomic force microscopy) to identify the proton conducting regions in a series of five phase-separated colpolymer materials [107]. They found that longer block lengths led to increased proton conductivity but did not necessarily correlate with fuel cell performance.

VIIIb. Lateral force microscopy

Although most primary uses of the AFM rely on the ability of the photodetector to detect the vertical motion of the cantilever, many photodetectors also have the ability to detect horizontal deflection of the reflected laser beam. Horizontal deflection of the optical path arises due to torsional bending of the cantilever. Such motion can be used to detect lateral vibrations of the cantilever [108-110], but is more commonly used to detect tip-sample friction in lateral force microscopy (LFM) [66, 111, 112]. In LFM, the AFM is operated in contact mode with the fast scan direction oriented perpendicular to the long axis of the cantilever. Friction between the tip and sample generates a lateral force that induces torsional bending of the cantilever. Higher friction results in increased torsional bending and lower friction results in less torsional

bending. Calibration of the LFM signal is separate from the flexural spring constant calibration and is discussed in detail elsewhere [113, 114]. The absolute friction force can be determined from one half of the difference between the LFM response in the forward and backward scan directions.

Brant et al. used LFM with chemically modified probe tips to characterize chemical heterogeneities on the surface of NF and RO membranes [115]. The probes were functionalized with methyl, carboxyl or hydroxyl groups to probe specific chemical interactions. The authors contended that the observed friction variations were primarily attributed to differences in adhesion, and thus the images could be used to locally map adhesive force. It was found that the carboxyl terminated tips revealed a high percentage of surface area coverage of high adhesion material on both membrane types. The methyl and hydroxyl functionalized tips revealed the largest fraction of moderate adhesion regions on the NF membrane and low adhesion regions on the RO membrane. Overall, the chemically modified probes revealed the significant surface heterogeneity in chemical properties that exists at the membrane surface and is obscured in traditional surface characterization techniques such as contact angle.

Wei and Overney used lateral force microscopy as a means of characterizing local gas diffusion in hydrated Nafion and zeolite membranes [116]. By using a custom-designed sample mount, the downstream side of a membrane could be characterized with LFM while the upstream side was pressurized. The authors found that as upstream pressure was linearly increased, the friction force linearly decreased. For the zeolite membranes, the friction drop per pressure

increase was directly proportional to the bulk flux of the membranes. For Nafion, this friction-pressure gradient was found to undergo a clear transition in the vicinity of 70 °C, almost 10 °C below the mechanical thermal transition determined for the unhydrated material. In subsequent work [117, 118], Overney's group found that the friction signal could be affected simultaneously by permeant-induced mechanical property changes in the material (e.g., plasticization) and the upward force of permeant molecules acting on the AFM tip.

VIIIc. Thermal AFM methods

Given the relation between the thermal transitions of a polymer and its performance, the integration of high-resolution thermal methods in the AFM is a powerful tool. There are three primary ways in which a sample can be heated in the AFM: heating of the ambient environment, direct heating of the sample or a heater beneath the sample [54], and direct local heating of the AFM probe itself [119, 120]. With environmental or sample heating, the AFM is operated just as at room temperature, although special care must be taken to ensure that temperature-sensitive components (e.g. the piezos) do not overheat. Local heating of the cantilever probe requires special instrumentation, including a cantilever with integrated resistive heater, and electronics to control current in the cantilever. Custom heated cantilevers were originally built by bending a micrometer-diameter wire to act as both the heater and probe [119]. This approach had severe limits regarding spatial resolution, which led to the development of microfabricated U-shaped probes with a low doped silicon region near the cantilever apex [120]. When current flows through the low doped region, heating occurs.

Because of the small thermal mass, the cantilevers are capable of very high heating rates and maximum temperatures > 500 °C. There is no risk to the AFM components because of the localized nature of the heat source. The heated probes can be used to detect material softening temperatures (e.g., melt or glass transition) by placing the probe at a prescribed sample location, then ramping the voltage to the probe until the height or deflection signal of the AFM indicates penetration of the probe into the material[119, 121]. The probes can also be used with conventional scanning techniques or as a means of surface manipulation and nanofabrication.

Killgore and Overney used heated-tip AFM (HT-AFM) to characterize the thermomechanical transition temperatures of a poly[(trimethylsilyl)propyne] gas separation material far from and in the vicinity of nanoparticle fillers [35, 36]. The bulk-like material was found to exhibit a very high transition temperature (> 300 °C), although corresponding transitions near a silica nanoparticle interface were depressed by ≈ 30 °C. The lower transition temperature in the interfacial material was attributed to locally increased free volume, which supports bulk observations of increased flux properties in nanocomposites of the polymer.

Maruf et al. also used HT-AFM to characterize membrane materials. They characterized the degradation of the polyamide layer in TFC RO membranes when exposed to chlorine [37]. Because of the thinness of the amide layer (< 200 nm), traditional thermal analysis techniques were not appropriate. The ability of HT-AFM to characterize such a thin material provides significant capabilities for membrane characterization. The authors found that the glass transition temperature of the membranes decreased monotonically with chlorine exposure

time and that transition temperature was very sensitive to the pH level of the chlorine solution. The reductions in transition temperature corresponded well with bulk decreases in salt rejection rate, showing the strong interrelation between nanoscale properties and bulk performance.

VIIId. Scanning Electrochemical Microscopy

Scanning electrochemical microscopy (SECM) is a form of scanning probe microscopy that can provide a localized image of electrochemical processes [122, 123]. SECM has shown significant promise in the characterization of ion flux in porous materials, and is thus quite relevant to membrane characterization. As capabilities advance, SECM is expected to play an increasingly important role. The early SECMs were custom-built, standalone instruments that bore relatively little relation to the AFM; however, later developments saw the integration of SECM and AFM into a single instrument platform. A standalone SECM has similar rastering requirements as AFM, but the cantilever and tip are replaced by a sharpened ultramicroelectrode (UME). Additional electrodes are located at the substrate and in a reference electrolyte. When the UME is brought close to a conducting surface, oxidizable species are reduced and a detectable current is produced at the UME. A bipotentiostat controls the tip and substrate potentials. A number of operation modes are possible, depending on the conductivity of the substrate and whether the tip or sample is acting as the electroactive species donor or generator. The combined SECM-AFM operates in a similar manner to the standalone SECM, except that the UME is integrated with the cantilever [124]. SECM-AFM

probes were first fabricated by bending the UME, then flattening a segment of the wire to

produce a cantilever with quasi-rectangular cross-section that neatly transitions into a UME tip

with a circular cross section. Other fabrication methods have involved modification of

traditional AFM probes, integration of carbon nanotubes, or direct microfabrication. As the tips

become sharper and less disc-like at their apex, spatial resolution is increased, but quantitative

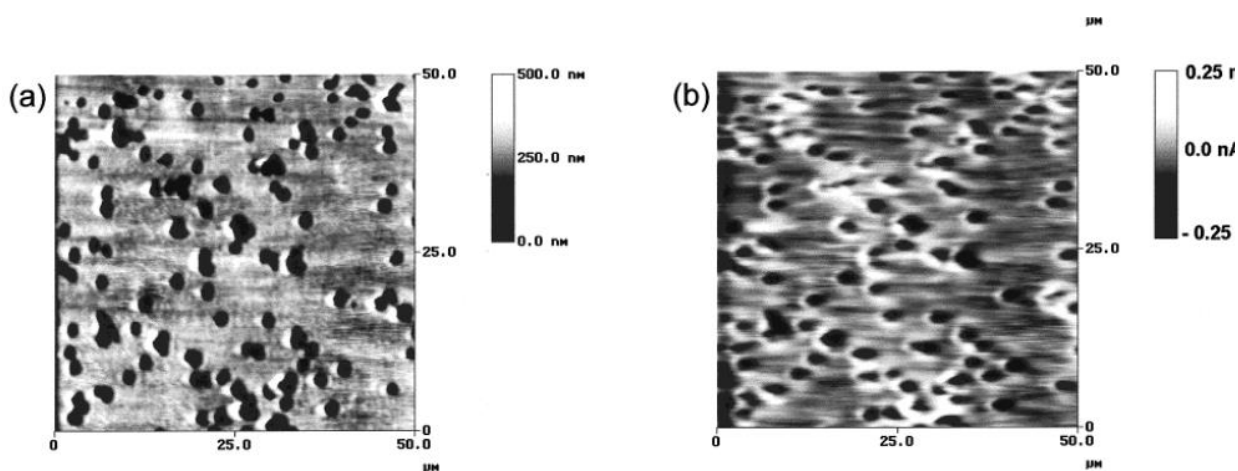reaction kinetics become more difficult to determine.

Figure X.10: Simultaneously acquired SECM-AFM images of (a) topography and (b) SECM

current on a track etched membrane. From [125]

Scott et al. were the first to demonstrate the local imaging of ion flux in porous materials with

SECM [126]. They utilized a porous mica membrane with track-etched, ~1 µm pores through its

thickness. A $Fe(CN)_6^{-4}$ electrolyte was placed in the donor compartment of the membrane

assembly, and SECM was used to image the receptor side. The resultant current images

showed clear circular features with increased faradic current in a lower current background.

Evidence of single pore specificity was observed when individual pores that initially exhibited a

high current switched off after time, indicating obstruction of the diffusion path. Subsequent

studies made additional progress in imaging flux across human skin and dentin membranes

[127].   However, the higher resolution required for imaging flux in ultrafiltration (UF), NF or RO

membranes was lacking. The combined SECM-AFM showed significant promise for addressing

this deficiency.   The first use of SECM-AFM was demonstrated on a track-etched membrane

similar to that used for standalone SECM [125]. The membrane separated a $IrCl_6$ –KCl-H_2O

donor phase from a KCl-H_2O receptor phase.   Unlike the standalone SECM that could identify

only pores with active transport occurring, SECM-AFM provided simultaneous topography and

current information. Figure X.10 shows the simultaneously acquired topography (a) and

current (b) images of the surface. Whereas all pores appear nominally similar in the

topography image, the current image reveals pores with obvious high and low current,

attributed to different amounts of ion diffusion. With increased refinement of the method, the

same authors demonstrated SECM-AFM detection of single pores < 100 nm in diameter and

separated by ≈ 250 nm [128]. The highest resolution pore transport SECM has recently been

reported by Shen et al. [129] By outfitting the SECM with a nanopipette tip ≈ 15 nm in

diameter, the authors were able to image ion conductance in pores as small as 40 nm diameter,

and separated by less than 60 nm center to center.   In addition to characterizing porous

materials, SECM variants have also proven successful for the characterization of proton

transport in Nafion fuel cell membranes. Aleksandrova et al. used conductive electrochemical

AFM to identify ≈ 10 nm ion channels in the membranes [30]. Clear heterogeneities and

temporal fluctuation in proton transport have also been observed, challenging existing

transport models [31].

IX. Summary

The AFM is a highly versatile tool for nanoscale surface characterization and has shown great promise in membrane science. The most basic functions of the tool, high-resolution topographic imaging and force versus distance spectroscopy, have aided in an improved fundamental understanding of membrane structure, performance, and lifetime. Moving forward, increasingly advanced AFM and SPM capabilities that can reveal chemical, mechanical, and real time flux information are likely to have an important role in advancing membrane characterization. Instrument advancements in the AFM continue to occur at a rapid pace, with new abilities to measure properties that could never have been measured before. Future needs will determine which of these capabilities are adopted by the membrane science community.

X. Further Learning

Users are encouraged to read the references provided in this chapter as well as attend technical conferences for more information. Leaders in AFM research and AFM instrument vendors typically have strong exhibition and symposium showings at the Material Research Society spring and fall meetings, the American Vacuum Society International Symposium, the Biophysical society Meeting, the American Physical Society March Meeting and the American Chemical Society meetings. There are also a number of AFM specific meetings including the International Scanning Probe Microscopy meeting, Multifrequency AFM, Non-contact AFM, Scanning Probe Microscopy of Soft and Polymeric Materials, Seeing at the Nanoscale, and others.

XI. Acknowledgements

XII. References

1. G.K. Binnig, C.F. Quate, and C. Gerber, Atomic force microscope, Physical Review Letters, 56, 930-933 (1986).

2. F.J. Giessibl, Atomic resolution of the silicon (111)-(7x7) surface by atomic force microscopy, Science, 267, 68-71 (1995).

3. S.C. Minne, et al., Centimeter scale atomic force microscope imaging and lithography, Applied Physics Letters, 73, 1742-1744 (1998).

4. G. Binnig and H. Rohrer, Scanning tunneling microscopy, IBM Journal of Research and Development, 44, 279-293 (2000).

5. A. Lewis, et al., Development of a 500 Å spatial resolution light microscope: I. light is efficiently transmitted through $\lambda/16$ diameter apertures, Ultramicroscopy, 13, 227-231 (1984).

6.   A. Avila and B. Bhushan, Electrical measurement techniques in atomic force microscopy, Critical Reviews in Solid State and Materials Sciences, 35, 38-51 (2010).

7.   H.-J. Butt, B. Cappella, and M. Kappl, Force measurements with the atomic force microscope: Technique, interpretation and applications, Surface Science Reports, 59, 1-152 (2005).

8.   S.-I. Nakao, Determination of pore size and pore size distribution, Journal of Membrane Science, 96, 131-165 (1994).

9.   S. Wang, G. Guillen, and E.M.V. Hoek, Direct observation of microbial adhesion to membranes., Environmental Science & Technology, 39, 6461-9 (2005).

10.   M. Elimelech, et al., Role of membrane surface morphology in colloidal fouling of cellulose acetate and composite aromatic polyamide reverse osmosis membranes, Journal of Membrane Science, 127, 101-109 (1997).

11.   W.R. Bowen and T.A. Doneva, Atomic force microscopy studies of membranes: Effect of surface roughness on double-layer interactions and particle adhesion., Journal of Colloid and Interface Science, 229, 544-549 (2000).

12.   E.M. Vrijenhoek, S. Hong, and M. Elimelech, Influence of membrane surface properties on initial rate of colloidal fouling of reverse osmosis and nanofiltration membranes, Journal of Membrane Science, 188, 115-128 (2001).

13.   S.S. Madaeni, Effect of surface roughness on retention of reverse osmosis membranes, Journal of Porous Materials, 11, 255-263 (2004).

14.   K. Boussu, et al., Roughness and hydrophobicity studies of nanofiltration membranes using different modes of AFM., Journal of Colloid and Interface Science, 286, 632-8 (2005).

15.   S. Al-Jeshi and A. Neville, An investigation into the relationship between flux and roughness on RO membranes using scanning probe microscopy, Desalination, 189, 221-228 (2006).

16. C. Hobbs, J. Taylor, and S. Hong, Effect of surface roughness on fouling of RO and NF membranes during filtration of a high organic surficial groundwater, Journal of Water Supply: Research and Technology—AQUA, 55, 559 (2006).

17. I. Koyuncu, et al., A comparison of vertical scanning interferometry (VSI) and atomic force microscopy (AFM) for characterizing membrane surface topography, Journal of Membrane Science, 278, 410-417 (2006).

18. S. Pal, et al., Evaluation of surface roughness of a plasma treated polymeric membrane by wavelet analysis and quantification of its enhanced performance, Applied Surface Science, 255, 2504-2511 (2008).

19. P.C.Y. Wong, Y.-N. Kwon, and C.S. Criddle, Use of atomic force microscopy and fractal geometry to characterize the roughness of nano-, micro-, and ultrafiltration membranes, Journal of Membrane Science, 340, 117-132 (2009).

20. Z. Zhong, et al., Membrane surface roughness characterization and its influence on ultrafine particle adhesion, Separation and Purification Technology, 90, 140-146 (2012).

21. W.R. Bowen, et al., Atomic force microscope studies of membranes: Surface pore structures of Cyclopore and Anopore membranes, Journal of Membrane Science, 110, 233-238 (1996).

22. W.R. Bowen and N. Hilal, Visualisation of an ultrafiltration membrane by non-contact atomic force microscopy at single pore resolution, Journal of Membrane Science, 110, 229-232 (1996).

23. W.R. Bowen, et al., Atomic force microscope studies of membranes: Surface pore structures of diaflo ultrafiltration membranes, Journal of Colloid and Interface Science, 180, 350-359 (1996).

24. W.R. Bowen and T.A. Doneva, Atomic force microscopy characterization of ultrafiltration membranes: correspondence between surface pore dimensions and molecular weight cut-off, Surface and Interface Analysis, 29, 544-547 (2000).

25. N.A. Ochoa, et al., Pore size distributions based on AFM imaging and retention of multidisperse polymer solutes: Characterisation of polyethersulfone UF membranes with dopes containing different PVP, Journal of Membrane Science, 187, 227-237 (2001).

26. M. Khayet and T. Matsuura, Determination of surface and bulk pore sizes of flat-sheet and hollow-fiber membranes by atomic force microscopy, gas permeation and solute transport methods, Desalination, 158, 57-64 (2003).

27. N. Hilal, et al., Characterisation of nanofiltration membranes using atomic force microscopy, Desalination, 177, 187-199 (2005).

28. J. Stawikowska and A.G. Livingston, Assessment of atomic force microscopy for characterisation of nanofiltration membranes, Journal of Membrane Science, 425-426, 58-70 (2013).

29. E. Aleksandrova, et al., Proton conductivity study of a fuel cell membrane with nanoscale resolution, ChemPhysChem, 8, 519-22 (2007).

30. E. Aleksandrova, et al., Electrochemical atomic force microscopy study of proton conductivity in a Nafion membrane., Physical Chemistry Chemical Physics : PCCP, 9, 2735-43 (2007).

31. R. Hiesgen, et al., High-resolution imaging of ion conductivity of Nafion® membranes with electrochemical atomic force microscopy, Electrochimica Acta, 55, 423-429 (2009).

32. R. Hiesgen, et al., Nanoscale properties of polymer fuel cell materials — A selected review, International Journal of Energy Research, 1223-1238 (2010).

33. E. Aleksandrova, et al., Spatial distribution and dynamics of proton conductivity in fuel cell membranes: potential and limitations of electrochemical atomic force microscopy measurements., Journal of Physics: Condensed Matter 23, 234109 (2011).

34. M. Hara, et al., Imaging individual proton-conducting spots on sulfonated multiblock-copolymer membrane under controlled hydrogen atmosphere by current-sensing atomic force microscopy., The Journal of Physical Chemistry. B, 117, 3892-9 (2013).

35.   T. Gray, et al., Molecular mobility and transitions in complex organic systems studied by shear force microscopy, Nanotechnology, 18, 044009 (2007).

36.   J.P. Killgore and R.M. Overney, Interfacial mobility and bonding strength in nanocomposite thin film membranes., Langmuir, 24, 3446-51 (2008).

37.   S.H. Maruf, et al., Correlation between barrier layer Tg and a thin-film composite polyamide membrane's performance: Effect of chlorine treatment, Journal of Membrane Science, 405-406, 167-175 (2012).

38.   W.R. Bowen, et al., A new technique for membrane characterisation: direct measurement of the force of adhesion of a single particle using an atomic force microscope, Journal of Membrane Science, 139, 269-274 (1998).

39.   W.R. Bowen, et al., Characterisation of membrane surfaces: direct measurement of biological adhesion using an atomic force microscope, Journal of Membrane Science, 154, 205-212 (1999).

40.   J.A. Brant and A.E. Childress, Colloidal adhesion to hydrophilic membrane surfaces, Journal of Membrane Science, 241, 235-248 (2004).

41.   S. Lee and M. Elimelech, Relating organic fouling of reverse osmosis membranes to intermolecular adhesion forces., Environmental Science & Technology, 40, 980-7 (2006).

42.   R. Bernstein, S. Belfer, and V. Freger, Bacterial attachment to RO membranes surface-modified by concentration-polarization-enhanced graft polymerization., Environmental Science & Technology, 45, 5973-80 (2011).

43.   R. Hiesgen, et al., Microscopic Analysis of Current and Mechanical Properties of Nafion(r) Studied by Atomic Force Microscopy, Membranes, 2, 783-803 (2012).

44.   R. Hiesgen, et al., Atomic force microscopy and infrared analysis of aging processes of polymer electrolyte membrane fuel cell components, Journal of Electroanalytical Chemistry, 662, 240-250 (2011).

45.   A. Pakzad, J. Simonsen, and R.S. Yassar, Elastic properties of thin poly(vinyl alcohol)-cellulose nanocrystal membranes., Nanotechnology, 23, 085706 (2012).

46.   K. Umemura, et al., Direct observation of deformation of nafion surfaces induced by methanol treatment by using atomic force microscopy, Applied Surface Science, 254, 7980-7984 (2008).

47.   T.J. Young, et al., The use of the PeakForce TM quantitative nanomechanical mapping AFM-based method for high-resolution Young's modulus measurement of polymers, Measurement Science and Technology, 22, 125703 (2011).

48.   T.R. Albrecht and C.F. Quate, Atomic resolution imaging of a nonconductor by atomic force microscopy, Journal of Applied Physics, 62, 2599-2602 (1987).

49.   O. Wolter, T. Bayer, and J. Greschner, Micromachined silicon sensors for scanning force microscopy, Journal of Vacuum Science & Technology B, 9, 1353-1357 (1991).

50.   T.R. Albrecht, et al., Microfabrication of cantilever styli for the atomic force microscope, Journal of Vacuum Science & Technology A: Vacuum, Surfaces, and Films, 8, 3386-3396 (1990).

51.   J. Liu, et al., Preventing nanoscale wear of atomic force microscopy tips through the use of monolithic ultrananocrystalline diamond probes., Small, 6, 1140-1149 (2010).

52.   D. Rugar, H.J. Mamin, and P. Guethner, Improved fiber-optic interferometer for atomic force microscopy, Applied Physics Letters, 55, 2588-2590 (1989).

53.   M. Tortonese, R.C. Barrett, and C.F. Quate, Atomic resolution with an atomic force microscope using piezoresistive detection, Applied Physics Letters, 62, 834-836 (1993).

54.   J. Broekmaat and A. Brinkman, High temperature surface imaging using atomic force microscopy, Applied Physics Letters, 23-25 (2008).

55.   W. Allers, et al., A scanning force microscope with atomic resolution in ultrahigh vacuum and at low temperatures, Review of Scientific Instruments, 69, 221-225 (1998).

56.   N.A. Burnham, et al., Comparison of calibration methods for atomic-force microscopy cantilevers, Nanotechnology, 14, 1 (2003).

57.   E.D. Langlois, et al., Spring constant calibration of atomic force microscopy cantilevers with a piezosensor transfer standard, Review of Scientific Instruments, 78, 093705-10 (2007).

58.   J.L. Hutter and J. Bechhoefer, Calibration of atomic-force microscope tips, Review of Scientific Instruments, 64, 1868 (1993).

59.   H.J. Butt and M. Jaschke, Calculation of thermal noise in atomic force microscopy, Nanotechnology, 6, 1 (1995).

60.   A. Torii, et al., A method for determining the spring constant of cantilevers for atomic force microscopy, Measurement Science and Technology, 7, 179 (1996).

61.   C.T. Gibson, G.S. Watson, and S. Myhra, Determination of the spring constants of probes for force microscopy/spectroscopy, Nanotechnology, 7, 259 (1996).

62.   R.S. Gates and M.G. Reitsma, Precise atomic force microscope cantilever spring constant calibration using a reference cantilever array, Review of Scientific Instruments, 78, 086101-3 (2007).

63.   C.A. Clifford and M.P. Seah, Improved methods and uncertainty analysis in the calibration of the spring constant of an atomic force microscope cantilever using static experimental methods, Measurement Science and Technology, 20, 125501 (2009).

64.   J.P. Cleveland, et al., A nondestructive method for determining the spring constant of cantilevers for scanning force microscopy, Review of Scientific Instruments, 64, 403-405 (1993).

65.   J.S. Villarrubia, Algorithms for scanned probe microscope image simulation, surface reconstruction, and tip estimation, Journal of Research of the National Institute of Standards and Technology, 102, 425-454 (1997).

66. C.M. Mate, et al., Atomic-scale friction of a tungsten tip on a graphite surface, Physical Review Letters, 59, 1942-1945 (1987).

67. S.J. O'shea, et al., Conducting atomic force microscopy study of silicon dioxide breakdown, Journal of Vacuum Science & Technology B, 13, 1945-1952 (1995).

68. U. Rabe and W. Arnold, Acoustic microscopy by atomic force microscopy, Applied Physics Letters, 64, 1493 (1994).

69. O.M. Leung and M.C. Goh, Orientational Ordering of Polymers by Atomic Force Microscope Tip-Surface Interaction, Science, 255, 64-66 (1992).

70. A. Khurshudov and K. Kato, Wear of the atomic force microscope tip under light load, studied by atomic force microscopy, Ultramicroscopy, 60, 11-16 (1995).

71. Q. Zhong, et al., Fractured polymer/silica fiber surface studied by tapping mode atomic force microscopy, Surface Science Letters, 290, L688-L692 (1993).

72. R. Garcia and R. Perez, Dynamic atomic force microscopy methods, Surface Science Reports, 47, 197-301 (2002).

73. W. Han, S.M. Lindsay, and T. Jing, A magnetically driven oscillating probe microscope for operation in liquids, Applied Physics Letters, 69, 4111-4113 (1996).

74. N. Umeda, S. Ishizaki, and H. Uwai, Scanning attractive force microscope using photothermal vibration, Journal of Vacuum Science & Technology B, 9, 1318-1322 (1991).

75. D. Kiracofe, et al., High efficiency laser photothermal excitation of microcantilever vibrations in air and liquids, Review of Scientific Instruments, 82, 013702-7 (2011).

76. S.N. Magonov, V. Elings, and M.H. Whangbo, Phase imaging and stiffness in tapping-mode atomic force microscopy, Surface Science, 375, L385-L391 (1997).

77. J. Tamayo and R. GarcíA, Relationship between phase shift and energy dissipation in tapping-mode scanning force microscopy, Applied Physics Letters, 73, 2926 (1998).

78.   R. Proksch and D.G. Yablon, Loss tangent imaging: Theory and simulations of repulsive-mode tapping atomic force microscopy, Applied Physics Letters, 100, 073106 (2012).

79.   R. García and A. San Paulo, Attractive and repulsive tip-sample interaction regimes in tapping-mode atomic force microscopy, Physical Review B, 60, 4961-4967 (1999).

80.   T.R. Albrecht, et al., Frequency modulation detection using high-Q cantilevers for enhanced force microscope sensitivity, Journal of Applied Physics, 69, 668-673 (1991).

81.   K.L. Westra and D.J. Thomson, Effect of tip shape on surface roughness measurements from atomic force microscopy images of thin films, Journal of Vacuum Science & Technology B, 13, 344 (1995).

82.   D.L. Sedin and K.L. Rowlen, Influence of tip size on AFM roughness measurements, Applied Surface Science, 182, 40-48 (2001).

83.   Y. Chen and W. Huang, Numerical simulation of the geometrical factors affecting surface roughness measurements by AFM, Measurement Science and Technology, 15, 2005-2010 (2004).

84.   M. Hirose, H. Ito, and Y. Kamiyama, Effect of skin layer surface structures on the flux behaviour of RO membranes, Journal of Membrane Science, 121, 209-215 (1996).

85.   Q. An, et al., Influence of polyvinyl alcohol on the surface morphology, separation and anti-fouling performance of the composite polyamide nanofiltration membranes, Journal of Membrane Science, 367, 158-165 (2011).

86.   P. Dietz, et al., Surface pore structures of micro- and ultrafiltration membranes imaged with the atomic force microscope, Journal of Membrane Science, 65, 101-111 (1992).

87.   P. Dietz, et al., Atomic-force microscopy of synthetic ultrafiltration membranes in air and under water, Ultramicroscopy, 35, 155-159 (1991).

88.   A.K. Fritzsche, et al., The structure and morphology of the skin of polyethersulfone ultrafiltration membranes: A comparative atomic force microscope and scanning electron microscope study, Journal of Applied Polymer Science, 45, 1945-1956 (1992).

89.   W.R. Bowen and T.A. Doneva, Artefacts in AFM studies of membranes: correcting pore images using fast fourier transform filtering, Journal of Membrane Science, 171, 141-147 (2000).

90.   B.V. Derjaguin, V.M. Muller, and Y.P. Toporov, Effect of contact deformations on the adhesion of particles, Journal of Colloid and Interface Science, 53, 314-326 (1975).

91.   K.L. Johnson, K. Kendall, and A.D. Roberts, Surface energy and the contact of elastic solids, Proceedings of the Royal Society of London. A. Mathematical and Physical Sciences, 324, 301-313 (1971).

92.   W.C. Oliver and G.M. Pharr, Measurement of hardness and elastic modulus by instrumented indentation: Advances in understanding and refinements to methodology, Journal of Materials Research, 19, 3-20 (2004).

93.   A.E. Childress, et al., *Evaluation of Membrane Characterization Methods*. 2012: Denver, CO. p. 154.

94.   N. Hilal, et al., A comprehensive review of nanofiltration membranes:Treatment, pretreatment, modelling, and atomic force microscopy, Desalination, 170, 281-308 (2004).

95.   Q. Li and M. Elimelech, Organic fouling and chemical cleaning of nanofiltration membranes: measurements and mechanisms., Environmental Science & Technology, 38, 4683-93 (2004).

96.   J.A. Brant and A.E. Childress, Membrane–colloid interactions: Comparison of extended DLVO predictions with AFM force measurements, Environmental Engineering Science, 19, 413-427 (2002).

97.   B.P. Frank and G. Belfort, Polysaccharides and sticky membrane surfaces: critical ionic effects, Journal of Membrane Science, 212, 205-212 (2003).

98.   K. Yamazaki, T. Yakushiji, and K. Sakai, Nanoscale analysis of hydrophilicity–hydrophobicity distribution on inner surfaces of wet dialysis membranes by atomic force microscopy, Journal of Membrane Science, 396, 38-42 (2012).

99.   D.T. Lee, J.P. Pelz, and B. Bhushan, Instrumentation for direct, low frequency scanning capacitance microscopy, and analysis of position dependent stray capacitance, Review of Scientific Instruments, 73, 3525-3533 (2002).

100.   M. Nonnenmacher, M.P. O'boyle, and H.K. Wickramasinghe, Kelvin probe force microscopy, Applied Physics Letters, 58, 2921-2923 (1991).

101.   S.V. Kalinin and D.A. Bonnell, Scanning impedance microscopy of electroactive interfaces, Applied Physics Letters, 78, 1306-1308 (2001).

102.   S.V. Kalinin and D.A. Bonnell, Imaging mechanism of piezoresponse force microscopy of ferroelectric surfaces, Physical Review B, 65, 125408 (2002).

103.   R. O'hayre, et al., Quantitative impedance measurement using atomic force microscopy, Journal of Applied Physics, 96, 3540-3549 (2004).

104.   K. Kanamura, H. Morikawa, and T. Umegaki, Observation of interface between Pt electrode and Nafion membrane, Journal of The Electrochemical Society, 150, A193 (2003).

105.   D.A. Bussian, et al., Nanoscale current imaging of the conducting channels in proton exchange membrane fuel cells., Nano Letters, 7, 227-32 (2007).

106.   X. Xie, et al., Local probe and conduction distribution of proton exchange membranes., The journal of physical chemistry. B, 111, 6134-40 (2007).

107.   N. Takimoto, et al., Conductive area ratio of multiblock copolymer electrolyte membranes evaluated by e-AFM and its impact on fuel cell performance, Journal of Power Sources, 194, 662-667 (2009).

108.   R.W. Carpick, D.F. Ogletree, and M. Salmeron, Lateral stiffness: A new nanomechanical measurement for the determination of shear strengths with friction force microscopy, Applied Physics Letters, 70, 1548 (1997).

109.   K.J. Wahl and S. Stepnowski, Viscoelastic effects in nanometer-scale contacts under shear, Tribology Letters, 5, 2-5 (1998).

110.   R.M. Overney, et al., Glass and structural transitions measured at polymer surfaces on the nanoscale, Journal of Thermal Analysis and Calorimetry, 59, 205-225 (2000).

111.   R.M. Overney, et al., Force microscopy study of friction and elastic compliance of phase-separated organic thin films, Langmuir, 10, 1281-1286 (1994).

112.   R.W. Carpick and M. Salmeron, Scratching the surface: Fundamental investigations of tribology with atomic force microscopy, Chemical Reviews, 97, 1163-1194 (1997).

113.   D.F. Ogletree, R.W. Carpick, and M. Salmeron, Calibration of frictional forces in atomic force microscopy, Review of Scientific Instruments, 67, 3298 (1996).

114.   M. Munz, Force calibration in lateral force microscopy: a review of the experimental methods, Journal of Physics D: Applied Physics, 43, 063001 (2010).

115.   J.A. Brant, K.M. Johnson, and A.E. Childress, Characterizing NF and RO membrane surface heterogeneity using chemical force microscopy, Colloids and Surfaces A: Physicochemical and Engineering Aspects, 280, 45-57 (2006).

116.   J.H. Wei, M. He, and R.M. Overney, Direct measurement of nanofluxes and structural relaxations of perfluorinated ionomer membranes by scanning probe microscopy, Journal of Membrane Science, 279, 608-614 (2006).

117.   J.P. Killgore and R.M. Overney. *Characterizing Membrane Sorption and Diffusion with Flux Lateral Force Microscopy*. in *NSTI BioNano*. Boston, MA (2008).

118.   D.B. Knorr, L.S. Kocherlakota, and R.M. Overney, Insight into reverse selectivity and relaxation behavior of poly[1-(trimethylsilyl)-1-propyne] by flux-lateral force and intrinsic friction microscopy, Journal of Membrane Science, 346, 302-309 (2010).

119.   A. Hammiche, et al., Highly localized thermal, mechanical, and spectroscopic characterization of polymers using miniaturized thermal probes, Journal of Vacuum Science & Technology B, 18, 1322 (2000).

120.   W.P. King, et al., Atomic force microscope cantilevers for combined thermomechanical data writing and reading, Applied Physics Letters, 78, 1300-1302 (2001).

121.   B.A. Nelson and W.P. King, Measuring material softening with nanoscale spatial resolution using heated silicon probes, Review of Scientific Instruments, 78, 023702 (2007).

122.   A.J. Bard, et al., Scanning electrochemical microscopy. Introduction and principles, Analytical Chemistry, 61, 132-138 (1989).

123.   P. Sun, F.O. Laforge, and M.V. Mirkin, Scanning electrochemical microscopy in the 21st century, Physical Chemistry Chemical Physics, 9, 802-823 (2007).

124.   C.E. Gardner and J.V. Macpherson, Atomic force microscopy probes go electrochemical, Analytical Chemistry, 74, 576 A-584 A (2002).

125.   J.V. Macpherson and P.R. Unwin, Combined scanning electrochemical-atomic force microscopy., Analytical Chemistry, 72, 276-85 (2000).

126.   E. Scott, H. White, and J.B. Phipps, Scanning electrochemical microscopy of a porous membrane, Journal of Membrane Science, 58, 71-87 (1991).

127.   S. Nugues and G. Denuault, Scanning electrochemical microscopy : amperometric probing of diffusional ion fluxes through porous membranes and human dentine, Journal of Electroanalytical Chemistry, 408, 125-140 (1996).

128. J.V. Macpherson, et al., Electrochemical imaging of diffusion through single nanoscale pores, Analytical Chemistry, 74, 1841-8 (2002).

129. M. Shen, et al., Quantitative imaging of ion transport through single nanopores by high-resolution scanning electrochemical microscopy, Journal of the American Chemical Society, 134, 9856-9 (2012).